Slow slip events and megathrust coupling changes reveal the earthquake potential before the 2020 Mw 7.4 Huatulco, Mexico event

Authors: Carlos Villafuerte[1]*, V. M. Cruz-Atienza[2], J. Tago[3], D. Solano-Rojas[3], R. Garza-Girón[4], S. I. Franco[2], L. A. Dominguez[5] and V. Kostoglodov[2].

November 2020

Affiliations

[1]Posgrado en Ciencias de la Tierra, Instituto de Geofísica, Universidad Nacional Autónoma de México, Mexico City, Mexico.

[2]Instituto de Geofísica, Universidad Nacional Autónoma de México, Mexico City, Mexico.

[3]Facultad de Ingeniería, Universidad Nacional Autónoma de México, Mexico City, Mexico.

[4]Department of Earth and Planetary Sciences, University of California, Santa Cruz, USA.

[5]Escuela Nacional de Estudios Superiores, Campus Morelia, Universidad Nacional Autónoma de México, Mexico.

*Correspondence to: villafuerte.cd@gmail.com

ABSTRACT

Stress accumulation on the plate interface of subduction zones is a key parameter that controls the location, timing and rupture characteristics of earthquakes. The diversity of slip processes occurring in the megathrust indicates that stress is highly variable in space and time. Based on GPS and InSAR data, we study in depth the evolution of the interplate slip-rate along the Oaxaca subduction zone, Mexico, from December 2016 through August 2020, with particular emphasis on the pre-seismic, coseismic and post-seismic phases associated with the June 23, 2020 Mw 7.4 Huatulco earthquake to understand how different slip processes contribute to the stress accumulation in the region. Unlike two time-invariant interplate coupling models previously proposed for the region, our results show that continuous changes in both the stress-releasing aseismic slip and the coupling produced a high stress concentration (i.e. Coulomb Failure Stress (CFS) of 700 ± 100 kPa) over the main asperity of the Huatulco earthquake and a stress shadow zone in the adjacent updip region (i.e. shallower than 17 km depth with CFS around -500 kPa). These findings may explain both the downdip rupture propagation (between 17 and 30 km depth) and its impediment to shallower, tsunamigenic interface regions, respectively. Interplate coupling time variations in the 2020 Huatulco and the nearby 1978 (Mw 7.8) Puerto Escondido rupture zones clearly correlate with the occurrence of the last three Slow Slip Events (SSEs) in Oaxaca far downdip of both zones, suggesting that SSEs are systematically accompanied by interplate coupling counterparts in the seismogenic zone that in turn have their own potentially-seismogenic stress and frictional implications. In the same period, the interface region of the 1978 event experienced a remarkably high CFS built-up of 1,000-1,700 kPa, half imparted by the co-seismic and early post-seismic slip of the neighboring Huatulco rupture, indicating large earthquake potential near Puerto Escondido. Continuous monitoring of the interplate slip-rate thus provides a better estimation of the stress accumulation in the seismogenic regions than those given by time-invariant coupling models and

improves our understanding of the megathrust mechanics where future earthquakes are likely to occur.

MAIN TEXT

1. Introduction

Large earthquakes occur along subduction zones in regions known as asperities (Lay and Kanamori, 1981), which represent locked areas of the interplate contact where frictional resistance allows elastic stress to build up during tens to hundreds of years as a consequence of the relative plate motion. Under the simple concept of Coulomb failure criterion, an earthquake occurs when the shear stress overcomes the strength of the fault. Both stressing-rate and fault strength are parameters that vary in time and space during the megathrust earthquake cycle (Moreno et al., 2011). Therefore, understanding the tectonic processes that cause these variations is essential to assess the seismic hazard in subduction zones.

Inter-seismic coupling maps obtained from geodetic observations have been widely used to identify heterogenous, highly locked segments of the plate interface where large earthquakes take place (Chlieh et al., 2008; Loveless and Meade, 2011; Moreno et al., 2010; Perfettini et al., 2010). Most of these estimations consider a steady-state long term deformation during the inter-seismic periods that results in a time invariant locking pattern. However, it has been observed that interplate coupling also varies with time (Heki and Mitsui, 2013; Melnick et al., 2017) and might be caused by different processes such as pore pressure transients (Cruz-Atienza et al., 2018; Materna et al., 2019; Warren-Smith et al., 2019) or dynamic stresses from regional earthquakes (Cruz-Atienza et al., 2020; Delorey et al., 2015; Materna et al., 2019).

69 During the inter-seismic period, a broad spectrum of tectonic processes occurs on the plate interface
70 with distinctive spatiotemporal characteristics that play an important role to accommodate the strain
71 along the megathrust. Among these processes, short-term and long-term slow slip events (SSEs),
72 which are aseismic slip transients lasting from days to months, release the strain accumulation in
73 the deeper and shallower segments of the plate interface (Beroza and Ide, 2011; Saffer and Wallace,
74 2015). Since their discovery, observations and theoretical models have proposed that SSEs increase
75 the stress in the adjacent seismogenic zone and may trigger damaging earthquakes (Obara and Kato,
76 2016; Segall and Bradley, 2012; Uchida et al., 2016; Voss et al., 2018). Moreover, it has been
77 documented that major interplate earthquakes in different subduction zones are preceded by SSEs,
78 although the actual mechanisms of their interaction remain under debate.
79
80 In the Mexican subduction zone, the recurrence of Mw 7+ interplate earthquakes is ~30–50 years
81 (Singh et al., 1981). In the deeper segment of the megathrust (30-50 km depth), long-term SSEs
82 occur in Oaxaca and Guerrero with recurrence of 1.5 and 3.5 years, respectively (Cotte et al., 2009;
83 Graham et al., 2016). The last four Mw 7+ interplate events in the Mexican subduction zone were
84 preceded by SSEs in the downdip adjacent region: The 2014 Mw 7.4 Papanoa earthquake in
85 Guerrero (Radiguet et al., 2016) and three more in Oaxaca, the 2012 Mw. 7.5 Ometepec earthquake
86 (Graham et al., 2014a), the 2018 Mw 7.2 Pinotepa earthquake (Cruz-Atienza et al., 2020) and, as it
87 will be shown later, the 2020 Mw 7.4 Huatulco earthquake. These observations suggest that the
88 prevalent mechanism of the interaction between SSEs and unstable shallower regions in the
89 Mexican subduction zone is the stress loading from adjacent slow slip processes. Although SSEs
90 do not always trigger large earthquakes, they do interact periodically with the updip locked regions,
91 thus contributing with the total stress built-up of the seismogenic zone.
92

93 Three years before the 2020 Huatulco earthquake, a complex sequence of SSEs and devastating
94 earthquakes took place from June 2017 to July 2019 in central and southern Mexico, including the
95 Mw 8.2 Tehuantepec and Mw 7.1 Puebla-Morelos earthquakes in 2017, and the Mw 7.2 Pinotepa
96 earthquake in 2018, describing a cascade of events interacting with each other on a regional scale
97 via quasi-static and/or dynamic perturbations (Cruz-Atienza et al., 2020). In Oaxaca, the plate
98 interface slipped (aseismically) almost continuously for the whole two years period with at least
99 two reactivations, one during the post-seismic relaxation of the Mw 7.2 Pinotepa earthquake, and
00 the second one with the 2019 Oaxaca SSE.
01
02 Here we thoroughly study the evolution of the interplate slip-rate history in the Oaxaca segment
03 during this unprecedented sequence including the pre-seismic, coseismic and post-seismic phases
04 of the 2020 Huatulco earthquake with the aim of understanding how these processes contribute to
05 the seismic potential in the region. We show that the continuous and simultaneous monitoring of
06 SSEs and the megathrust coupling provides a better estimation of the stress accumulation on the
07 locked regions where future large earthquakes are expected to occur.
08
09 ## 2. The 2020 Mw 7.4 Huatulco Earthquake
10
11 ### 2.1 Coseismic slip inversion
12
13 On June 23, 2020, a shallow Mw 7.4 interplate thrust earthquake took place below the state of
14 Oaxaca, Mexico (Fig. 1), with relocated hypocentral coordinates (15.822º, -96.125º, 17.2 km,
15 determined from seismic records at the station HUAT of the Mexican Servicio Sismológico
16 Nacional (SSN), which is 7 km south of the epicenter) within the aftershock area of the 1965 Mw
17 7.5 earthquake, the last interplate rupture in this region (Chael and Stewart, 1982).

We combined nearfield GPS and Interferometric Synthetic Aperture Radar (InSAR) data to obtain the coseismic slip distribution by means of ELADIN, a newly developed adjoint inversion method (Tago et al., 2020) (see Supplementary Materials). For the GPS data we used high rate (1 s) time series to measure the coseismic static displacement at four stations near the epicenter (Figs. 1c and S1c-f). The displacement in Huatulco (HUAT station), the closest epicentral site, was carefully and independently estimated using GPS, tide gauge and strong motion data, yielding very consistent values of 49 cm uplift and 40 cm seaward displacement (Figs. S1b and S1c). The InSAR line-of-sight (LOS) displacement map (Figs. 1b and S2) was generated from scenes taken before the earthquake, on June 19, and two days after the earthquake, on June 25, by the Sentinel satellite of the European Space Agency on ascending track 107. The InSAR data processing is described in the Supplementary Materials. For all slip inversions presented in this work we assumed the 3D plate interface geometry introduced by Cruz-Atienza et al. (2020) and discretized it, for the coseismic solutions, into subfaults with planar square projections of 5 x 5 km^2.

To determine the optimal data weights for the joint inversion of GPS and InSAR data we first inverted each data set individually. Both independent solution models produced almost a perfect data fit but significantly different slip distributions, as shown in Figs. S3a and S3b (see Supplementary Materials). Numoerous joint inversion tests led us to optimal data weights (Supplementary Materials) producing a final solution that owns the most prominent features of both independent models and satisfactorily explains the whole set of observations, with average GPS and InSAR data errors of 1.2 ± 1.0 cm and 0.2 ± 2.1cm, respectively (Figs. 1 and S3c).

Fig. 1a features our preferred coseismic slip solution with two main patches, the most prominent downdip the hypocenter, between 21 and 32 km depth with peak value of 3.4 m, and a second one

45 km east-northeast, almost below the coast (peak value of 1.8 m), which differs from a recently published solution (Melgar et al., 2020) that did not integrate the closest (GPS and strong motion) data and estimated a static uplift in Huatulco 6 cm higher than ours. Our slip solution explains both the uplift and seaward displacement there, and shows that no significant slip (i.e. larger than 1 m) took place offshore (Fig. S3c). Furthermore, it clearly suggests a rupture directivity towards the north-northeast, essentially downdip from the hypocenter. Two more features stand out from our model: 1) The rupture ends abruptly updip and very close to the nucleation point. 2) The downdip slip limit might correspond to the end of the locked segment of the megathrust, as observed for the 2018 Pinotepa Earthquake (Li et al., 2020) and the aftershocks areas of regional interplate earthquakes (white patches in Fig. 1).

Whether the 2020 Huatulco earthquake is a repetition of two previous events that occurred in 1928 (Ms 7.6) and 1965 (Ms 7.4) is an important matter that goes beyond the scope of this work. However, since this question can be addressed by comparing far-field waveforms of the earthquakes, which are sensitive to the source depth (Chael and Stewart, 1982; Singh et al., 1984), we performed a supplementary inversion exercise where the interface was shifted 3.5 km upward to match our relocated hypocentral depth. The inversion yielded similar source characteristics as described above (Fig. S4) with some differences discussed in the Supplementary Materials that do not have a significant bearing on any subsequent analysis.

2.2 The 2020 Oaxaca SSE that preceded the earthquake

Two months before the Huatulco earthquake, on mid-April 2020, three GPS stations in Oaxaca (TNNP, TNNX and OAXA) changed their typical interseismic motion from roughly northeast to southwest, indicating a transient deformation associated with a SSE (light blue section in Figs. 2a

and S6a). We used continuous displacement records on 12 permanent GPS stations in Oaxaca belonging to the SSN and Tlalocnet (Cabral-Cano et al., 2018), between September 2019 and the Huatulco earthquake date (Fig. S5) to simultaneously invert for the plate interface coupling (PIC) and any stress-releasing slip episode (e.g. SSEs) in successive time windows using ELADIN (Fig. 2). For these and the next inversions, the 3D plate interface was discretized with coarser subfaults of 10 x 10 km^2.

Fig. 2e shows the main slow slip patch downdip of the 1978 Puerto Escondido earthquake region, between 25 and 50 km depth, with an equivalent moment magnitude Mw 6.4 (Mo = 7.914 x 10^{18} N*m assuming a shear modulus of 32 GPa). The location and magnitude of this SSE are consistent with previously reported SSEs in Oaxaca (Correa-Mora et al., 2008; Cruz-Atienza et al., 2020; Graham et al., 2016). It is also clear that the SSE did not penetrate the rupture area of the Huatulco earthquake. Instead, we observe a remarkable PIC evolution previous to the event in that area, where the interface decoupled around February-March (Fig. 2d) before getting fully coupled just before the earthquake (i.e. during the strongest SSE phase, Fig. 2e). This can also be seen directly in the GPS time series at the stations closest to the epicenter, such as OXUM and HUAT (Fig. 2a), where we do not observe the SSE southward rebound before the earthquake. In contrast, the displacement trends present a slight acceleration to the north. Something similar occurred in the hypocentral region of the 2018 Pinotepa earthquake 200 km west, where the seismicity rate also increased in the two months preceding the rupture (Cruz-Atienza et al., 2020). We carefully analyzed the foreshock seismicity starting from August 2016 in the hypocentral region of the Huatulco earthquake using the one-station template-matching procedure introduced by Cruz-Atienza et al. (2020) using continuous broadband records at the HUIG station (Fig. S7). However, unlike the observations of the 2018 Pinotepa earthquake, we did not find significant increase in the seismicity rate before the event that could shed light on the rupture initiation mechanism.

Although the transient deformation produced by the SSE is noticeable from mid-April, the inter-SSE displacement trends in some stations started changing well before, around mid-February as observed in Fig. 2a, suggesting a gradual plate interface decoupling process at a regional scale preceding the SSE-induced crustal relaxation, which can be observed in Figs. 2b-2d (and Supplementary Movie S1). Before this process began (Fig. 2b), the downdip segment of the plate interface, between 25-50 km, was fully coupled while small SSE episodes were taking place in both the 2018 Pinotepa earthquake area and up-dip of the Huatulco earthquake rupture zone. In the following two months, there seems to have been an incipient downdip SSE propagation from south to north in Pinotepa along with another small relaxation to the east of the area where the long-term SSE will develop (Supplementary Movie S1 and Figs. 2b-2c). Then, in Fig. 2d we see how the segment downdip of the 1978 earthquake area is the last one to experience a PIC reduction (i.e. the interface slip starts accelerating but always below the plate convergence rate) leading to the main SSE patch occurrence in April-June, the months preceding the earthquake (Fig. 2e). All of these observations clearly demonstrate the regional-wide preparatory phase for the 2020 Oaxaca SSE.

A common practice to isolate the deformation associated with slow slip transients is to subtract the inter-SSE linear trend from the GPS time series. The residual deformation is then assumed to correspond to the strain released by the SSE (e.g., (Bartlow et al., 2011; Hirose et al., 2014; Radiguet et al., 2011)). When one does this to invert for the slip at the interface, the preparatory phase of the SSE (i.e. the slow decoupling process preceding the SSE relaxation) is mapped/interpreted as aseismic slip resulting in an elastic crustal rebound (i.e. a stress drop), which is not really correct. This assumption leads to systematic overestimations of the SSE related displacements and thus the equivalent seismic moment with relevant implications in the scaling

properties of slow earthquakes and, more importantly, in the slip budget over several SSE cycles, which may be significantly underestimated.

2.3 Early post-seismic deformation

We inverted the early post-seismic GPS displacements (i.e. the first 2 months discretized in 6 ten-day windows, Figs. 3a and S6b) produced by the mainshock using the same parameterization for the ELADIN method as in the previous section. We then assumed that such displacements are only due to the afterslip on the plate interface, which is a reasonable approximation considering that the viscoelastic relaxation after a similar thrust event 260 km west, the 2012 (Mw 7.5) Ometepec earthquake, was negligible in a post-seismic period three times longer (Graham et al., 2014b).

Four main observations arise from the afterslip evolution of the Huatulco earthquake (Fig. 3b and Supplementary Movie S1): (1) the largest afterslip concentrates between 20 and 50 km depth involving also the main SSE patch occurred before the earthquake (i.e. downdip from the 1978 rupture area) and where previous SSEs have been identified (Fig. S8); (2) the maximum postslip area completely overlaps with the coseismic rupture area; (3) the afterslip spreads offshore up to the oceanic trench where most of aftershocks were concentrated; and (4) the afterslip rate reaches its maximum value of 390 cm/year during the first 10 days following the event.

The complete overlap of coseismic and postseismic slip has been observed in the last three interplate thrust earthquakes (Mw > 7) in Oaxaca, the 2012 (Mw 7.5) Ometepec (Graham et al., 2014b); the 2018 (Mw 7.2) Pinotepa (Cruz-Atienza et al., 2020) and the 2020 (Mw 7.4) Huatulco (this study) events, indicating that these seismogenic segments of the plate interface, with the depth range between 10 and 30 km, can release elastic strain energy both seismically and aseismically. The peak

afterslip velocity of the Huatulco event reported above is almost seven times higher than the one of the Pinotepa earthquake (Supplementary Movie S2) (Cruz-Atienza et al., 2020), suggesting significant lateral differences in the mechanical properties along the Oaxaca subduction zone.

The cumulative aseismic moment released during the first two months following the earthquake was 1.808 x 10^{20} N*m, equivalent to a moment magnitude Mw 7.44, which is 24% larger than the coseismic moment. The high postseismic/coseismic moment ratio is also a common feature of the three Oaxaca events mentioned above, that significantly differs from the much lower estimate for the 2014 (Mw 7.4) Papanoa thrust earthquake in Guerrero, where the aseismic postslip moment was 30% smaller than the corresponding coseismic value (Gualandi et al., 2017).

One of the most noteworthy features of the postseismic process in the region is that the Huatulco earthquake postslip did not penetrate the rupture area of the 1978 Puerto Escondido earthquake (dashed ellipse in Fig. 3b), which remained fully coupled during the two-month period. Unlike the preseismic phase, the PIC in the 1978 rupture area abruptly increased just after the earthquake (compare Figs. 2 and 3) suggesting significant dynamic implications in terms of the postseismic strain accommodation in the region.

3. Interplate slip-rate evolution in the Oaxaca subduction zone.

Before the occurrence of the Huatulco earthquake, a complex sequence of earthquakes and SSEs took place in an unusual way along the Mexican subduction zone from April 2017 to September 2019 (Cruz-Atienza et al., 2020). During the sequence, the plate interface experienced remarkable changes of the PIC in the whole megathrust over time (see Supplementary Movie S2). Fig. 4 summarizes two examples of these remarkably changes where high coupled regions (PIC > 0.6)

67 evolve before (green patches) and after (warm color patches) the Pinotepa and Huatulco
68 earthquakes.
69
70 We analyze the evolution of the aseismic slip along the Oaxaca megathrust before the Huatulco
71 earthquake by using the slip history inverted by Cruz-Atienza et al. (2020) (from December 2016
72 to September 2019) and the sequence inverted here before the Huatulco earthquake (Fig. 2), linearly
73 interpolated every 30 days. Fig. 5a shows the evolution of the total aseismic slip on the plate
74 interface along the trench (i.e. projected into the green lines of Fig. 4) averaged between 10-30 km
75 depth, which include the segments of the 2018 Pinotepa, 1978 Puerto Escondido and 2020 Huatulco
76 earthquakes (Fig. 4). Thus, the difference between the final cumulative slip curve and the thick
77 dashed line, which represents the expected total displacement of the incoming Cocos plate during
78 the same period (DeMets et al., 2010), can be interpreted as the slip deficit along the trench in this
79 particular period.
80
81 We disaggregated the plate interface aseismic total slip into the slip transients associated with SSE
82 and afterslip, i.e., those events that release elastic strain (Fig. 5b), and the slip that occurs under the
83 coupling regime, i.e., the interplate creep where the slip velocity is less than or equal to the plate
84 convergence rate (Fig. 5c). Fig. 5b shows that the afterslip contribution from the Pinotepa
85 earthquake dominates in the region, although there were SSEs in this segment before the earthquake
86 (blue to green areas below the red curve). There is also a portion of the Huatulco segment where
87 some small SSEs contribute to the total slip in the plate interface, while this contribution is
88 negligible in the 1978 rupture area.
89
90 The evolution of creeping (Fig. 5c) reveals strong variations of the slip velocity in different time
91 intervals along the whole Oaxaca segment indicating that the interplate coupling changes

92 significantly over time. Some of the most prominent changes of the PIC occur before and after
93 SSEs (e.g. black rectangles), as well as in the 1978 earthquake region during the post-seismic
94 deformation of both the Pinotepa and Huatulco earthquakes, as previously discussed in Figs. 2, 3
95 and 4.
96
97 To better analyze the interplate slip-rate variations we extracted the time series of the slip evolution
98 at four places of the plate interface (dashed circles with radius of 20 km in Fig. 4). Region A, over
99 the rupture area of the Huatulco earthquake; Region B, over the rupture area of the 1978 Puerto
00 Escondido earthquake estimated by Mikumo et al. (2002); Region C, updip from the Huatulco
01 earthquake where most of its aftershocks are located; and Region D, downdip from the rupture area
02 of the Puerto Escondido earthquake. Figs. 6 and S9a show the evolution of the mean total aseismic
03 slip (black line), the creeping (yellow line), the relaxing slip (red line) and the PIC (blue line) within
04 each of the four circular regions.
05
06 In the Huatulco rupture area (Region A, Fig. 6a), the contribution to the total slip is mainly due to
07 creeping except for a period after the Mw 8.2 Tehuantepec earthquake, when aseismic stress release
08 occurred on this patch. This 2017 SSE was indeed triggered by the quasistatic and dynamic stresses
09 produced by the great Tehuantepec event as demonstrated by (Cruz-Atienza et al., 2020). In this
10 region, PIC is highly variable over time and correlates remarkably well with the occurrence of
11 neighboring SSEs in Oaxaca even though these events did not penetrate the region. During the
12 occurrence of such regional SSEs, the PIC gradually decreases down to values of 0.2-0.4 and then
13 increases in the final stage of the SSEs to recover the relatively high values of 0.7-0.9 observed in
14 the inter-SSE periods. This behavior is very similar in Region D (Fig. S9a), downdip from the 1978
15 rupture area, except that PIC starts to recover after the end of the 2019 SSE.
16

In the 1978 rupture area (Region B, Fig. 6b) there is no evidence of aseismic stress release, so the total slip is only associated with creeping. Although it is not so clear as in Region A, this case is also characterized by large variations of the PIC that correlate with the occurrence of regional SSEs and postslip. There is for instance a great variation of the creeping rate before and after the Pinotepa earthquake, where the PIC raises from ~0.3 before the earthquake (during the final stage of the 2017 Oaxaca SSE) to almost 1.0 (fully coupled) just after the earthquake, and then gradually decreases to a low PIC value during the corresponding postseismic relaxation. Also notice the sharp growth of PIC in both regions A and B during the 2020 Oaxaca SSE just before the Huatulco earthquake.

Offshore (and updip) from the Huatulco earthquake (Region C, Fig. 6c) we find a more consistent low PIC value across the whole studied period with some exceptions after the Tehuantepec earthquake and just before the initiation of the 2020 SSE. The gap in the PIC curve between December 2018 and the end of March 2019 means that all subfaults within this region underwent a SSE. The red curve indicates that there are small and persistent SSEs in this offshore region over time, which is consistent with the significant afterslip developed there after the Huatulco earthquake that extended up to the trench. These observations suggest that the frictional properties of this region are prone to release aseismically a fraction of the accumulated stress.

4. Implications of SSEs and PIC changes on the stress built-up

Variations in the interplate aseismic slip rate have important implications for both friction and the stress build-up along the megathrust. We estimated the Coulomb Failure Stress (CFS) changes (Nikkhoo and Walter (2015), see Supplementary Materials) produced by the relaxing slip (SSEs and afterslip) and the interplate coupling to elucidate how the stress evolves along the Oaxaca segment. For this analysis we have also included the coseismic stresses imparted by the Pinotepa

and Huatulco earthquakes. Figs. 7a and 7b show the average cumulative CFS every 30 days from December 2017 up to the moment of the Huatulco event along the trench for two different depth ranges encompassing the rupture areas of the 2020 Huatulco (between 20 and 30 km depth) and the 1978 Puerto Escondido (between 10 and 20 km depth) earthquakes. It is important to note that these estimates of the CFS are the result of stress contributions from the whole plate interface and not just from the sub-faults delimited by the depth ranges.

As expected, the CFS cumulative rate is highly variable over time and along the trench. For the deeper band (Fig. 7a), we observe that despite the great variations of the slip-rate on the megathrust, the CFS in Huatulco always increased up to values ranging from 400 to 800 kPa. The same happens downdip of the 1978 rupture, where the cumulative CFS is even higher (between 800 kPa and 1 MPa). For the shallower band (Fig. 7b), the CFS decreases and remains negative right updip of the Huatulco rupture reaching values of ~-500 kPa. Such negative values are associated with the stress shadows produced by neighboring strong coupled segments (e.g. the 1978 earthquake area, Fig. 7c) and the periodic release of stress by short-term SSEs in this eastern segment (Figs. 2 and 7d). To the west, in the 1978 rupture area, we find the opposite situation. The CFS always increased to values between 200 and 500 kPa, which are approximately half of the CFS estimates downdip of this segment (Fig. 7a).

Fig. S10 shows both the long-term and inter-SSE time-invariant interplate coupling models estimated by Radiguet et al. (2016) together with their associated CFS change rate. Both models produce large stressing rates mainly in the highly coupled segment of the 1978 earthquake region. However, they also produce large stress shadows in the adjacent less coupled regions (both along-dip and along-strike) such as in the Pinotepa and Huatulco rupture zones. In contrast, our aseismic time-evolving slip-rate model predicts a very different scenario. Fig. 8a shows the cumulative CFS

67 at the time of the Huatulco earthquake including contributions of all aseismic slip processes imaged
68 in the megathrust during the 3.5 years preceding the event (from December 2016 to June 23, 2020).
69 A simple inspection reveals large differences in the stress build-up pattern with respect to the time-
70 invariant models, especially in both the Huatulco and Pinotepa rupture areas, and east-southeast of
71 the 1978 earthquake zone. The bottom four panels of Fig. 8 show the cumulative (trench-
72 perpendicular average) CFS along the trench for the same two bands with different depth ranges
73 analyzed earlier. The left column shows the cumulative CFS at the time of the Huatulco earthquake,
74 while the right column shows the same quantity plus the coseismic and postseismic stress
75 increments.
76
77 In the deeper band at the moment and within the rupture area of the Huatulco earthquake (Fig. 8b),
78 the CFS from our time-evolving slip model (blue area) indicates almost double the CFS predicted
79 by the inter-SSE coupling model (yellow area) and more than twice in the downdip region of the
80 1978 rupture area. On the contrary, the long-term coupling model (orange area) predicts negative
81 CFS values in Huatulco (i.e. no earthquake potential) and low positive values in the downdip region
82 of the 1978 rupture. When adding the CFS imparted by the Huatulco earthquake and its postseismic
83 afterslip (Fig. 8e), our estimate doubles up right downdip of the 1978 rupture area, from about 800
84 kPa to over 1.8 MPa. A significant fraction of this value is due to the persistently high coupling in
85 this region throughout the post-seismic phase (Fig. 3). This large segment west of the Huatulco
86 rupture (Region D in Fig. 8d) might be then very prone to a future earthquake, as has occurred in
87 neighboring regions over the deep part of the locked zone, where the last two interplate earthquakes
88 in Oaxaca (the Pinotepa and Huatulco events) took place with most of their seismic moment
89 released below 20 km (Li et al., 2020).
90

In the shallower band, the three models predict similar CFS values over the 1978 rupture area before the Huatulco rupture (Fig. 8c), although the inter-SSE model gives much higher values in the eastern part of the main patch. Between the 1978 and Huatulco ruptures areas, only our time-evolving model predicts a CFS deficit, which is fully compensated (reaching positive values around 800 kPa) by the coseismic and postseismic deformations produced by the Huatulco earthquake (Fig. 8f).

We can therefore distinguish three major differences between our time-evolving CFS estimates and those from the time-invariant coupling models: (1) very high stress concentration over the rupture area of the Huatulco earthquake predicted only by our model, (2) absolute CFS values between 20 and 30 km depth at least twice as high in our model, and (3) a large stress shadow zone updip the Huatulco rupture that is absent in both time-invariant models.

We now analyze in depth the CFS evolution in the Huatulco and 1978 rupture areas produced by our time-evolving interplate slip-rate model. Figs 9a and 9b show the total CFS evolution in both regions (black curves) together with the linear predictions given by the time-invariant coupling models of Radiguet et al. (2016) (green lines). To assess which slip process dominates the stress build-up, we also disaggregated the total CFS into the stress contributions produced by regions in coupling regime only (yellow curves) and by the relaxing slip only (red curves).

In the Huatulco rupture zone (Region A, Fig. 9a) our model shows a sustained growth of the total CFS during the 3.5 years prior to the rupture, reaching values close to 700 kPa and where 80% of the stress contribution comes from regions in coupling regime. The remaining 20% is mainly associated with the SSE occurred following the 2017 Tehuantepec earthquake. In contrast, the long-term time-invariant model predicts a sustained decrease of CFS that implies a continuous reduction

of the earthquake potential. On the other hand, while the inter-SSE time-invariant model predicts a growth of the CFS, the final value is about one third of what our model yields. Since the Huatulco earthquake took place, it seems that our time-evolving slip-rate model and its associated CFS clearly represents a more realistic description of the actual megathrust processes than any of the time-invariant coupling models analyzed here. This is also easily seen by comparing our CFS estimates in the hypocentral region at the time of the earthquake (Supplementary Movie S1 and Fig. 8a) with those produced by the time-invariant models (Fig. S10).

Considering the 1978 rupture zone (Region B, Fig. 9b), our model reveals significant temporal variations primarily controlled by the stress contributions from regions in coupling regime until they reach 400 kPa at the time of the Huatulco earthquake. The stress produced by SSEs at that time is ~100 kPa, which represents ~25% of the total CFS. For this specific region, while the inter-SSE time-invariant model predicts a cumulative stress that is almost twice our model's prediction, the long-term time-invariant model is close to our time-evolving cumulative value. When integrating the contributions from the coseismic and postseismic slip of the Huatulco earthquake, then our stress estimate gets close to the inter-SSE prediction with high CFS values around 800 kPa.

Fig. S11 presents the regional contributions to the CFS (Fig. 8a) of both relaxing slip and coupling separately. Although in very different proportions, both contributions promote an increase in earthquake potential in the rupture areas of the Huatulco and 1978 earthquakes. Figs. 9c and 9d show the percentages of these contributions only where the total CFS is positive in Fig. 8a (i.e. where there was an effective increase of the earthquake potential). We can see that both rupture zones (Regions A and B, Figs. 9a and 9b) are actually representative of the accumulation and partitioning of stresses between 10-35 km depth in all but the western segment of the region. We

can also see that although most of the accumulated stress (i.e. ~75-85%) was generated by coupled interface regions, 15-25% was due to SSEs and the Pinontepa earthquake afterslip occurring in the region over the 3.5 years period.

5. Discussion

The segment of the plate interface where the Huatulco earthquake ruptured has been characterized with moderate coupling (Fig. S10) (Radiguet et al., 2016; Rousset et al., 2016). Previous M7 class interplate earthquakes have occurred very close to it, such as the 1965 and 1928 events, suggesting a possible reactivation of the same asperity over time (Chael and Stewart, 1982; Singh et al., 1984). Historical data also suggest that two older, probably thrust earthquakes with magnitude larger than 7 occurred nearby in 1870 and 1801 (Suárez et al., 2020). Assuming that all these events broke the same plate interface patch, their average return period would be ~55 +/- 13 years. In this region also occurred the Mw ~8.6 San Sixto earthquake in 1787 over a ~300 km along-strike segment producing a great tsunami offshore Oaxaca (Suárez and Albini, 2009; Ramírez-Herrera et al., 2020). Such event must have involved the rupture of several locked segments along the Oaxaca megathrust including offshore shallow portions of the plate interface to generate the mega-tsunami. Whether M8+ events may repeat depends, among other factors, on the interplate friction and constructive stress interaction between different locked and unlocked fault segments (Kaneko et al., 2010; Kaneko et al., 2018), which continuously change over time. Recent laboratory experiments and theoretical fault models strongly suggest that the friction is a sensitive function of the interplate slip velocity where SSEs take place (Im et al., 2020). Then, since the slip velocity changes over time, these variations should be essential for the dynamic stability of the megathrust because of both their frictional counterparts and the associated stress changes documented here for the Oaxaca subduction zone. To have an insight into the actual earthquake potential (e.g. to assess whether

adjacent locked segments are likely to break jointly to produce a much larger event) it is therefore necessary a proper and continuous quantification of the stress accumulation as proposed here. Monitoring the interplate slip-rate continuously might also allow us to constrain the evolution of the frictional parameters that determine the slip stability regime on the megathrust.

An interesting feature of the Huatulco earthquake is that rupture did not propagate into the adjacent updip segment (above ~17 km depth) that should also be locked. Impeding the rupture propagation into that segment might be associated with the interface geometry (e.g. due to subducted plate reliefs as recently proposed in the Guerrero seismic gap (Plata-Martínez et al., 2020)), the frictional conditions and/or, as shown in this investigation, with the existence of a significantly-large stress barrier due to both the stress shadow produced by nearby strongly coupled zones and persistent small SSE occurring updip. The spatial distribution of aftershocks during the first 50 days following the Huatulco event is clearly shifted updip (about 30 km) from the rupture area, where the afterslip developed and the CFS strongly increased. Only very few aftershocks lie within the main slip patch, indicating an effective stress release within the most of the rupture area, which is consistent with other M7 class earthquakes observed worldwide (Wetzler et al., 2018). Furthermore, the earthquake nucleation in the shallowest part of the rupture zone and northward propagation can also be explained by our model due to the localized increments of CFS right in the nucleation zone over the six months prior to the earthquake (Supplementary Movie S1) and the longer-term stress accumulation downdip the hypocenter (Figs. 7a and 8a), respectively.

We find that strongly coupled regions in Oaxaca are highly variable in space and time before and after the occurrence of the Pinotepa and Huatulco earthquakes. These remarkable PIC variations might be associated with abrupt changes in the mechanical properties of the fault zone materials induced by the dynamic perturbations of the seismic waves from the earthquakes (Cruz-Atienza et

al., 2020; Materna et al., 2019). Furthermore, we observed that the PIC changes are somehow linked to nearby SSEs that occur in the region (Figs. 6a and S9a). To explain these short-term variations of the PIC at seismogenic depths, we favor models involving fluctuations of fluid pressure as proposed for the long-term SSEs in the Guerrero subduction zone (Cruz-Atienza et al., 2018), in southern Cascadia (Materna et al., 2019) and the Hikurangi subduction zone (Warren-Smith et al., 2019). Recently, models evoking the fault-valving concept show overpressure pulses migrating upward along the fault as the permeability evolves in the fault zone (Cruz-Atienza et al., 2018; Shapiro et al., 2018; Zhu et al., 2020). These transient changes in pore pressure may lead to large variations of the fault strength as high as ~10-20 MPa (Zhu et al., 2020), which makes this mechanism a plausible candidate to explain the strong PIC variations in the seismogenic zone of Oaxaca during the occurrence of SSEs and earthquakes.

Earthquake potential depends on the state of stress along the subduction zone that, as shown here, is a function of different evolving processes taking place from the trench to its deep portion where the plates mechanical interaction ceases. The stress build-up therefore changes over time and space in a complex way, so does the earthquake potential. Time-invariant estimates of the interplate coupling are often used to identify seismogenic segments that are prone to large earthquakes (Chlieh et al., 2008; Loveless and Meade, 2011; Moreno et al., 2010; Perfettini et al., 2010). However, while these estimates are certainly useful on a large spatial and temporal scale, they do not provide a reliable picture of the earthquake potential associated with smaller ($7 < M < 8.5$) but potentially devastating ruptures that occur more frequently, as shown in this work for the Oaxaca megathrust.

Our results indicate that continuously monitoring the interplate slip velocity provides a better reconstruction of the stress development on the seismogenic region. Systematic and simultaneous observation of PIC and the relaxing slip (SSE and afterslip) over the plate interface is thus very relevant to evaluate theoretical predictions of the interface dynamics, which is our leading approach

to understand the underlying physics in subduction systems.

6. Conclusions

We analyzed the interplate slip-rate evolution during 3.5 years in the Oaxaca subduction zone including the pre-seismic, coseismic and post-seismic phases associated with the June 23, 2020 Mw 7.4 Huatulco earthquake to understand how the different slip processes contribute to the plate-interface stress accumulation in the region. We found that the main rupture area of the Huatulco earthquake extents between 20 and 30 km depth with two main and compact slip patches, the most prominent north the hypocenter and a much smaller close to the coast, east-northeast of the hypocenter. The 2020 SSE that occurred before the earthquake did not penetrate the rupture area and was preceded by a gradual interface decoupling process at a regional scale, including the maximum SSE slip area. During the two months preceding to the earthquake, when the 2020 SSE developed, the Huatulco earthquake rupture area became fully locked. Our slip inversions indicate that the two-month earthquake afterslip overlapped the whole coseismic rupture area and propagated both to the trench and to the northwest, where most of aftershocks happened and where the 2020 SSE was developing as well as previous SSEs have occurred in the region, respectively. During the post-seismic phase, the rupture area of the 1978 Puerto Escondido earthquake became and remained fully coupled. The interplate slip-rate evolution in Oaxaca during the 3.5 years preceding the Huatulco earthquake shows that the PIC in the megathrust seismogenic region is highly variable in time and space, and that the PIC reductions over the Huatulco and the 1978 rupture areas are well correlated with the occurrence of SSEs further downdip, clearly suggesting a physical relationship between both processes. We found that both stress-relaxing aseismic slip events and megathrust coupling changes produced a region of high stress accumulation where the main asperity of the Huatulco earthquake broke as well as a shallow stress deficit region that

probably impeded the updip propagation of the earthquake. Our results suggest that continuous monitoring of the interplate aseismic slip-rate and its CFS counterpart provides a better estimation of the earthquake potential on locked seismogenic regions than predictions given by time-independent interplate coupling models. Finally, the stress imparted during the coseismic and postseismic phases of the Huatulco earthquake on the 1978 rupture area make it a region very prone to the next earthquake in the nearest future, which is consistent with the ~50 years earthquake return period in the Oaxaca region.

Declaration on competing or conflict of interest

The authors have no competing or conflict of interest in what is expressed in this manuscript.

CRediT authorship contribution statement

C. Villafuerte: Conceptualization, Methodology, Investigation, Formal Analysis, Writing-Original Draft, Visualization. **V.M. Cruz-Atienza:** Conceptualization, Methodology, Investigation, Visualization, Writing-Review & Editing, Supervision. **J. Tago:** Methodology, Investigation, Software, Validation, Review & Editing. **D. Solano-Rojas:** Investigation, Validation, Data processing, Review & Editing **R. Garza-Girón:** Investigation, Visualization, Data processing, Review & Editing **S.I. Franco:** Data processing, Editing. **L.A. Dominguez:** Investigation, Editing. **V. Kostoglodov:** Investigation, Review & Editing.

Acknowledgments

We are grateful for the outstanding technical support of Eduardo Murrieta and Luciano Díaz in the maintenance of the Gaia supercomputing platform, and Luis Salazar in the TLALOCNet field operations and stations maintenance. We also thank Shri Krishna Singh, Arturo Iglesias and Gerardo Suárez for fruitful discussion; the Servicio Sismológico Nacional (SSN), the Servicio

Mareográfico Nacional (SMN) and the Servicio de Geodesia Satelital, all of them from the Instituto de Geofísica-UNAM, for all GPS, strong motion and tide gauge data, as well as all their personnel for data acquisition and distribution; and the European Space Agency for access to the Sentinel1 data. This work is partially based on GPS data belonging also to TLALOCNet and services provided by the GAGE Facility, operated by UNAVCO, Inc., with support from the National Science Foundation and the National Aeronautics and Space Administration under NSF Cooperative Agreement EAR-1724794. All GPS data has been processed in the Laboratorio de Geodesia Satelital (LaGeos) of the Instituto de Geofísica-UNAM. This work was supported by CONACyT grants 6471 and 255308, UNAM-PAPIIT grants IN113814, IG100617 and IG100921, JICA-JST SATREPS-UNAM grant 15543611, UNAM-DGTIC grant LANCAD-312 and the graduate school scholarships by CONACyT.

79 **References**

80

81 Bartlow, N.M., Miyazaki, S.i., Bradley, A.M., Segall, P., 2011. Space-time correlation of slip and
82 tremor during the 2009 Cascadia slow slip event. Geophysical Research Letters 38.
83 Beroza, G.C., Ide, S., 2011. Slow Earthquakes and Nonvolcanic Tremor. Annual Review of Earth
84 and Planetary Sciences 39, 271-296.
85 Cabral-Cano, E., Pérez-Campos, X., Márquez-Azúa, B., Sergeeva, M.A., Salazar-Tlaczani, L.,
86 DeMets, C., Adams, D., Galetzka, J., Hodgkinson, K., Feaux, K., Serra, Y.L., Mattioli, G.S.,
87 Miller, M., 2018. TLALOCNet: A Continuous GPS-Met Backbone in Mexico for
88 Seismotectonic and Atmospheric Research. Seismological Research Letters 89, 373-381.
89 Chael, E.P., Stewart, G.S., 1982. Recent large earthquakes along the Middle American Trench and
90 their implications for the subduction process. Journal of Geophysical Research: Solid Earth
91 87, 329-338.
92 Chlieh, M., Avouac, J.P., Sieh, K., Natawidjaja, D.H., Galetzka, J., 2008. Heterogeneous coupling
93 of the Sumatran megathrust constrained by geodetic and paleogeodetic measurements.
94 Journal of Geophysical Research: Solid Earth 113.
95 Correa-Mora, F., DeMets, C., Cabral-Cano, E., Marquez-Azua, B., Diaz-Molina, O., 2008.
96 Interplate coupling and transient slip along the subduction interface beneath Oaxaca,
97 Mexico. Geophysical Journal International 175, 269-290.
98 Cotte, N., Walpersdorf, A., Kostoglodov, V., Vergnolle, M., Santiago, J.-A., Campillo, M., 2009.
99 Anticipating the Next Large Silent Earthquake in Mexico. Eos, Transactions American
00 Geophysical Union 90, 181-182.
01 Cruz-Atienza, V.M., Tago, J., Villafuerte, C., Wei, M., Garza-Girón, R., Dominguez, L.A.,
02 Kostoglodov, V., Nishimura, T., Franco, S., Real, J., 2020. Short-Term Interaction between
03 Silent and Devastating Earthquakes in Mexico. Earth and Space Science Open Archive, 53.

Cruz-Atienza, V.M., Villafuerte, C., Bhat, H.S., 2018. Rapid tremor migration and pore-pressure waves in subduction zones. Nature Communications 9, 2900.

Delorey, A.A., Chao, K., Obara, K., Johnson, P.A., 2015. Cascading elastic perturbation in Japan due to the 2012 M_w 8.6 Indian Ocean earthquake. Science Advances 1, e1500468.

DeMets, C., Gordon, R.G., Argus, D.F., 2010. Geologically current plate motions. Geophysical Journal International 181, 1-80.

Graham, S., DeMets, C., Cabral-Cano, E., Kostoglodov, V., Rousset, B., Walpersdorf, A., Cotte, N., Lasserre, C., McCaffrey, R., Salazar-Tlaczani, L., 2016. Slow Slip History for the MEXICO Subduction Zone: 2005 Through 2011. Pure and Applied Geophysics 173, 3445-3465.

Graham, S.E., DeMets, C., Cabral-Cano, E., Kostoglodov, V., Walpersdorf, A., Cotte, N., Brudzinski, M., McCaffrey, R., Salazar-Tlaczani, L., 2014a. GPS constraints on the 2011–2012 Oaxaca slow slip event that preceded the 2012 March 20 Ometepec earthquake, southern Mexico. Geophysical Journal International 197, 1593-1607.

Graham, S.E., DeMets, C., Cabral-Cano, E., Kostoglodov, V., Walpersdorf, A., Cotte, N., Brudzinski, M., McCaffrey, R., Salazar-Tlaczani, L., 2014b. GPS constraints on the Mw = 7.5 Ometepec earthquake sequence, southern Mexico: coseismic and post-seismic deformation. Geophysical Journal International 199, 200-218.

Gualandi, A., Perfettini, H., Radiguet, M., Cotte, N., Kostoglodov, V., 2017. GPS deformation related to the Mw 7.3, 2014, Papanoa earthquake (Mexico) reveals the aseismic behavior of the Guerrero seismic gap. Geophysical Research Letters 44, 6039-6047.

Heki, K., Mitsui, Y., 2013. Accelerated pacific plate subduction following interplate thrust earthquakes at the Japan trench. Earth and Planetary Science Letters 363, 44-49.

28 Hirose, H., Matsuzawa, T., Kimura, T., Kimura, H., 2014. The Boso slow slip events in 2007 and
29 2011 as a driving process for the accompanying earthquake swarm. Geophysical Research
30 Letters 41, 2778-2785.
31 Im, K., Saffer, D., Marone, C., Avouac, J.-P., 2020. Slip-rate-dependent friction as a universal
32 mechanism for slow slip events. Nature Geoscience 13, 705-710.
33 Kaneko, Y., Avouac, J.-P., Lapusta, N., 2010. Towards inferring earthquake patterns from geodetic
34 observations of interseismic coupling. Nature Geoscience 3, 363-369.
35 Kaneko, Y., Wallace, L.M., Hamling, I.J., Gerstenberger, M.C., 2018. Simple Physical Model for
36 the Probability of a Subduction- Zone Earthquake Following Slow Slip Events and
37 Earthquakes: Application to the Hikurangi Megathrust, New Zealand. Geophysical
38 Research Letters 45, 3932-3941.
39 Lay, T., Kanamori, H., 1981. An Asperity Model of Large Earthquake Sequences, Earthquake
40 Prediction, pp. 579-592.
41 Li, Y., Shan, X., Zhu, C., Qiao, X., Zhao, L., Qu, C., 2020. Geodetic Model of the 2018 Mw 7.2
42 Pinotepa, Mexico, Earthquake Inferred from InSAR and GPS Data. Bulletin of the
43 Seismological Society of America 110, 1115-1124.
44 Loveless, J.P., Meade, B.J., 2011. Spatial correlation of interseismic coupling and coseismic rupture
45 extent of the 2011 MW = 9.0 Tohoku-oki earthquake. Geophysical Research Letters 38.
46 Materna, K., Bartlow, N., Wech, A., Williams, C., Bürgmann, R., 2019. Dynamically Triggered
47 Changes of Plate Interface Coupling in Southern Cascadia. Geophysical Research Letters
48 46, 12890-12899.
49 Melgar, D., Ruiz-Angulo, A., Pérez-Campos, X., Crowell, B.W., Xu, X., Cabral-Cano, E.,
50 Brudzinski, M.R., Rodriguez-Abreu, L., 2020. Energetic Rupture and Tsunamigenesis
51 during the 2020 Mw 7.4 La Crucecita, Mexico Earthquake. Seismological Research Letters.

52 Melnick, D., Moreno, M., Quinteros, J., Baez, J.C., Deng, Z., Li, S., Oncken, O., 2017. The super-
53 interseismic phase of the megathrust earthquake cycle in Chile. Geophysical Research
54 Letters 44, 784-791.
55 Mikumo, T., Yagi, Y., Singh, S.K., Santoyo, M.A., 2002. Coseismic and postseismic stress changes
56 in a subducting plate: Possible stress interactions between large interplate thrust and
57 intraplate normal-faulting earthquakes. Journal of Geophysical Research: Solid Earth 107,
58 ESE 5-1-ESE 5-12.
59 Moreno, M., Melnick, D., Rosenau, M., Bolte, J., Klotz, J., Echtler, H., Baez, J., Bataille, K., Chen,
60 J., Bevis, M., Hase, H., Oncken, O., 2011. Heterogeneous plate locking in the South–Central
61 Chile subduction zone: Building up the next great earthquake. Earth and Planetary Science
62 Letters 305, 413-424.
63 Moreno, M., Rosenau, M., Oncken, O., 2010. 2010 Maule earthquake slip correlates with pre-
64 seismic locking of Andean subduction zone. Nature 467, 198-202.
65 Nikkhoo, M., Walter, T.R., 2015. Triangular dislocation: an analytical, artefact-free solution.
66 Geophysical Journal International 201, 1119-1141.
67 Obara, K., Kato, A., 2016. Connecting slow earthquakes to huge earthquakes. Science 353, 253-
68 257.
69 Perfettini, H., Avouac, J.-P., Tavera, H., Kositsky, A., Nocquet, J.-M., Bondoux, F., Chlieh, M.,
70 Sladen, A., Audin, L., Farber, D.L., Soler, P., 2010. Seismic and aseismic slip on the Central
71 Peru megathrust. Nature 465, 78-81.
72 Plata-Martínez, R., Ide, S., Shinohara, M., Garcia, E., Mizuno, N., Dominguez, L.A., Taira, T.a.,
73 Yamashita, Y., Toh, A., Yamada, T., Real, J., Husker, A., Cruz-Atienza, V.M., Ito, Y., 2020.
74 Shallow slow earthquakes to decipher future catastrophic earthquakes in the Guerrero
75 seismic gap. In review at Nature Communications.

76 Radiguet, M., Cotton, F., Vergnolle, M., Campillo, M., Valette, B., Kostoglodov, V., Cotte, N.,
77 2011. Spatial and temporal evolution of a long term slow slip event: the 2006 Guerrero Slow
78 Slip Event. Geophysical Journal International 184, 816-828.
79 Radiguet, M., Perfettini, H., Cotte, N., Gualandi, A., Valette, B., Kostoglodov, V., Lhomme, T.,
80 Walpersdorf, A., Cabral Cano, E., Campillo, M., 2016. Triggering of the 2014 Mw7.3
81 Papanoa earthquake by a slow slip event in Guerrero, Mexico. Nature Geoscience 9, 829-
82 833.
83 Ramírez-Herrera, M.-T., Corona, N., Cerny, J., Castillo-Aja, R., Melgar, D., Lagos, M.,
84 Goguitchaichvili, A., Machain, M.L., Vazquez-Caamal, M.L., Ortuño, M., Caballero, M.,
85 Solano-Hernandez, E.A., Ruiz-Fernández, A.-C., 2020. Sand deposits reveal great
86 earthquakes and tsunamis at Mexican Pacific Coast. Scientific Reports 10, 11452.
87 Rousset, B., Lasserre, C., Cubas, N., Graham, S., Radiguet, M., DeMets, C., Socquet, A., Campillo,
88 M., Kostoglodov, V., Cabral-Cano, E., Cotte, N., Walpersdorf, A., 2016. Lateral Variations
89 of Interplate Coupling along the Mexican Subduction Interface: Relationships with Long-
90 Term Morphology and Fault Zone Mechanical Properties. Pure and Applied Geophysics
91 173, 3467-3486.
92 Saffer, D.M., Wallace, L.M., 2015. The frictional, hydrologic, metamorphic and thermal habitat of
93 shallow slow earthquakes. Nature Geoscience 8, 594-600.
94 Segall, P., Bradley, A.M., 2012. Slow-slip evolves into megathrust earthquakes in 2D numerical
95 simulations. Geophysical Research Letters 39.
96 Shapiro, N.M., Campillo, M., Kaminski, E., Vilotte, J.-P., Jaupart, C., 2018. Low-Frequency
97 Earthquakes and Pore Pressure Transients in Subduction Zones. Geophysical Research
98 Letters 45, 11,083-011,094.

Singh, S.K., Astiz, L., Havskov, J., 1981. Seismic gaps and recurrence periods of large earthquakes along the Mexican subduction zone: A reexamination. Bulletin of the Seismological Society of America 71, 827-843.

Singh, S.K., Dominguez, T., Caştro, R., Rodriguez, M., 1984. P waveform of large, shallow earthquakes along the Mexican subduction zone. Bulletin of the Seismological Society of America 74, 2135-2156.

Suárez, G., Albini, P., 2009. Evidence for Great Tsunamigenic Earthquakes (M 8.6) along the Mexican Subduction Zone. Bulletin of the Seismological Society of America 99, 892-896.

Suárez, G., Ruiz-Barón, D., Chico-Hernández, C., Zúñiga, F.R., 2020. Catalog of Preinstrumental Earthquakes in Central Mexico: Epicentral and Magnitude Estimations Based on Macroseismic Data. Bulletin of the Seismological Society of America.

Tago, J., Cruz-Atienza, V.M., Villafuerte, C., Nishimura, T., Kostoglodov, V., Real, J., Ito, Y., 2020. Adjoint Slip Inversion under a Constrained Optimization Framework: Revisiting the 2006 Guerrero Slow Slip Event. Earth and Space Science Open Archive, 34.

Uchida, N., Iinuma, T., Nadeau, R.M., Bürgmann, R., Hino, R., 2016. Periodic slow slip triggers megathrust zone earthquakes in northeastern Japan. Science 351, 488-492.

Voss, N., Dixon, T.H., Liu, Z., Malservisi, R., Protti, M., Schwartz, S., 2018. Do slow slip events trigger large and great megathrust earthquakes? Science Advances 4, eaat8472.

Warren-Smith, E., Fry, B., Wallace, L., Chon, E., Henrys, S., Sheehan, A., Mochizuki, K., Schwartz, S., Webb, S., Lebedev, S., 2019. Episodic stress and fluid pressure cycling in subducting oceanic crust during slow slip. Nature Geoscience 12, 475-481.

Wetzler, N., Lay, T., Brodsky, E.E., Kanamori, H., 2018. Systematic deficiency of aftershocks in areas of high coseismic slip for large subduction zone earthquakes. Science Advances 4, eaao3225.

Zhu, W., Allison, K.L., Dunham, E.M., Yang, Y., 2020. Fault valving and pore pressure evolution in simulations of earthquake sequences and aseismic slip. Nature Communications 11, 4833.

Figures

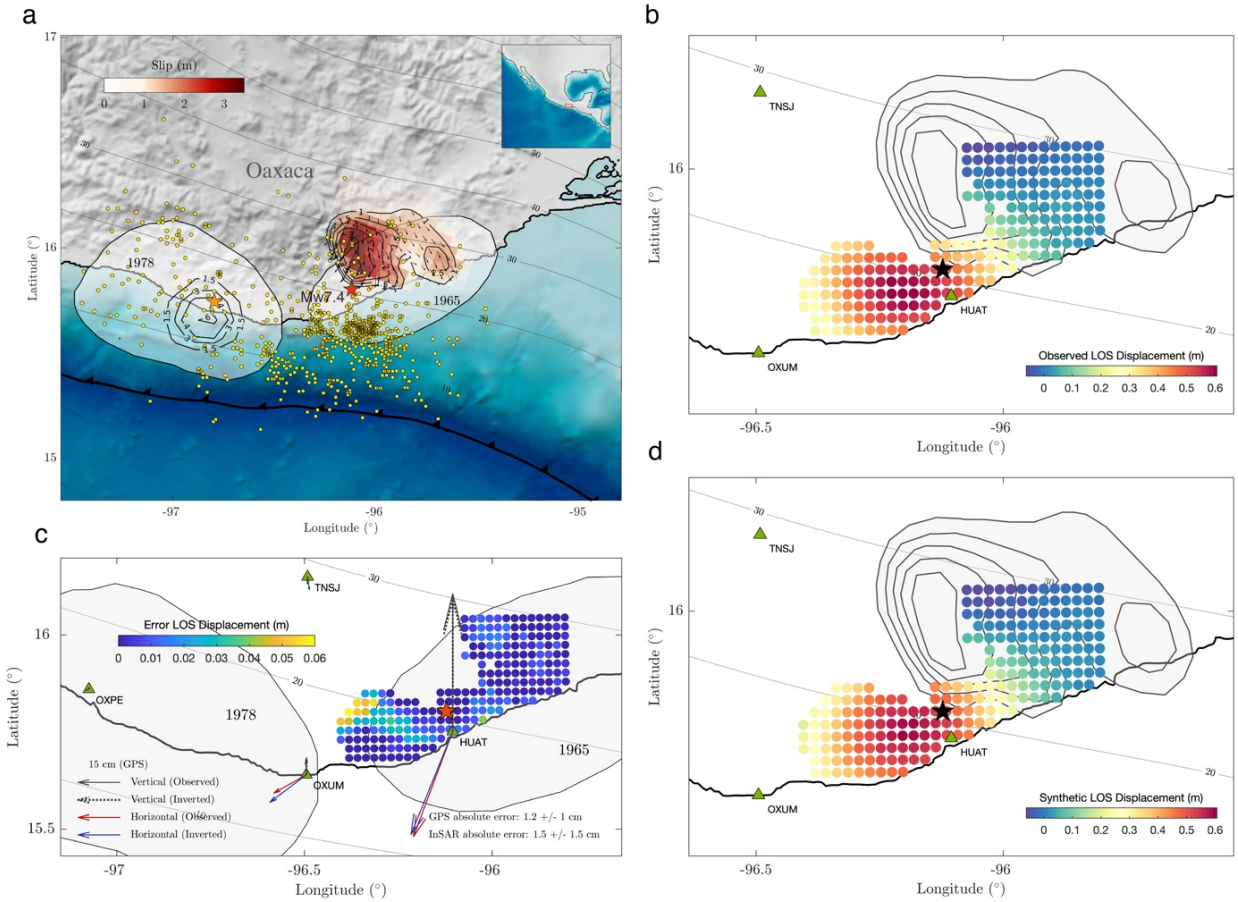

Fig. 1 Coseismic slip inversion results for the 2020 Mw 7.4 Huatulco earthquake. **a** Red colored region with black contours indicates the slip on the plate interface for our preferred joint GPS and InSAR slip inversion. Red and orange stars indicate the epicenters of the Huatulco and the 1978 Puerto Escondido earthquakes, respectively. Black contours around the 1978 Puerto Escondido hypocenter represent the 1.5, 3, 4 and 6 m slip isolines from Mikumo et al. (2002). White shaded patches show the aftershock areas of the historic interplate earthquakes in 1965 and 1978. Yellow dots depict the 50 days aftershocks reported by the SSN. Gray contours indicate the iso-depths of the 3D plate interface used for the slip inversions in this study. **b** and **d** show the observed and synthetic line of sight (LOS) displacements, respectively. **c** Misfit between observed and predicted LOS displacement and GPS surface displacements. Red and blue arrows show the observed and synthetic horizontal displacements from the GPS data. Continuous and dashed arrows indicate the observed and synthetic vertical displacement, respectively.

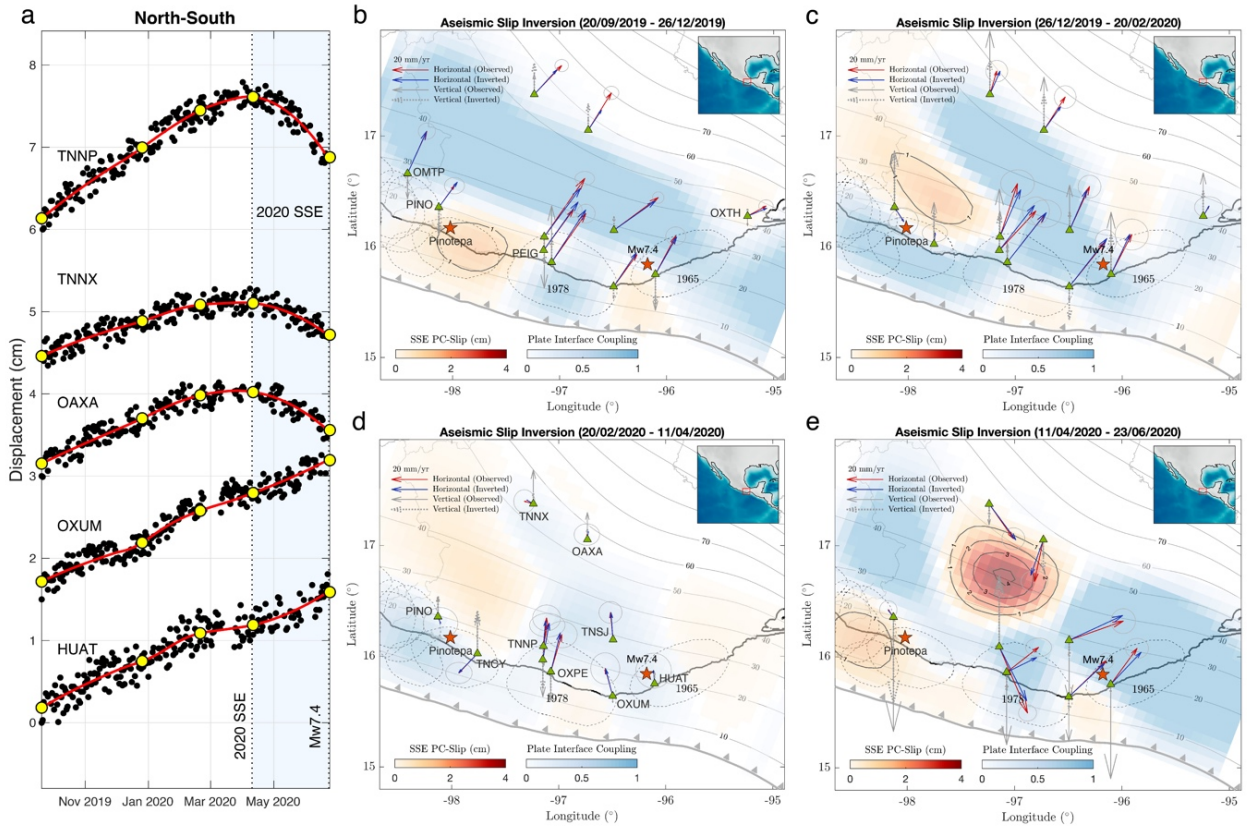

Fig. 2 GPS inversions of the pre-seismic deformation period during the two months preceding the Huatulco earthquake. **a** North-south displacement GPS time series in 5 selected stations. Yellow dots indicate the start and the end of the four time-windows used for the slip inversions shown in **b-e**. **b-e** Aseismic slip inversion for the 9 months deformation preceding the Huatulco earthquake. Red star depicts the epicenter of the earthquake. Slip contours are in centimeters. Dashed regions are the aftershock areas of historic interplate earthquakes. Red and blue arrows show the observed and synthetic horizontal displacements and the gray ellipses are their one standard deviations. Solid and dashed arrows indicate the observed and synthetic vertical displacement, respectively.

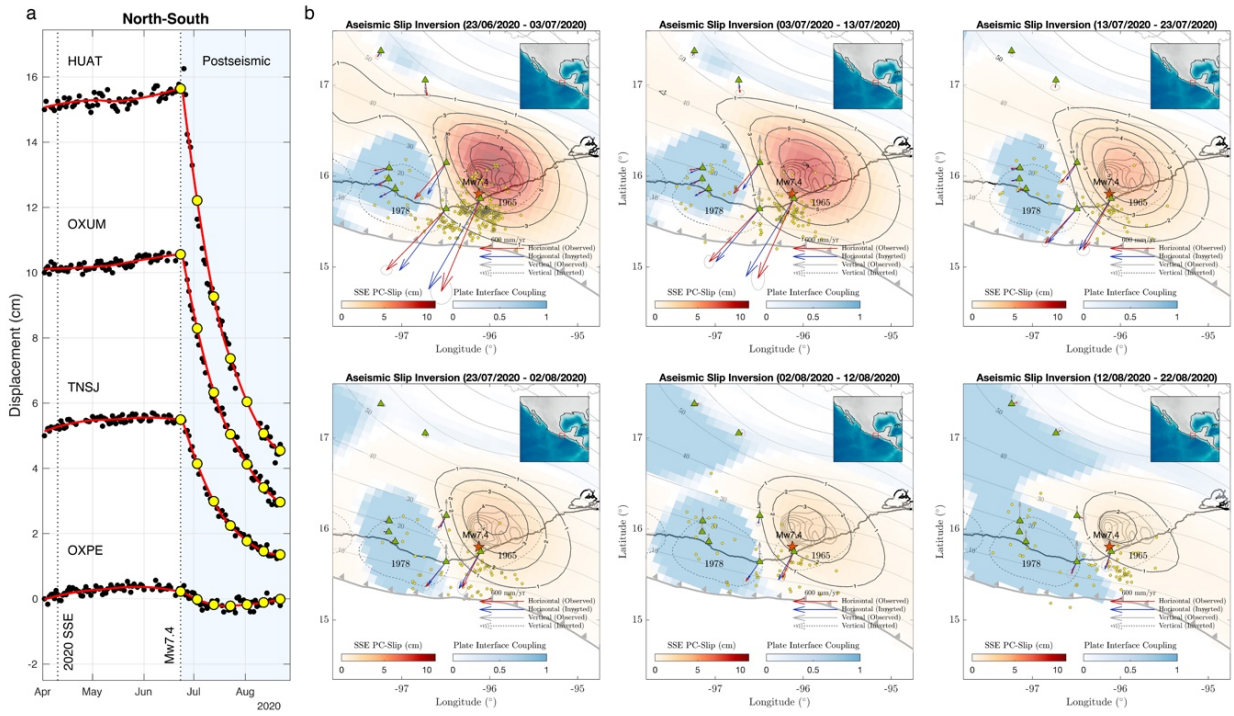

Fig. 3 GPS inversion of the postseismic deformation of the Huatulco earthquake. **a** North-south displacement GPS time series in 4 selected stations. Yellow dots indicate the start and the end of the six 10-day windows used for the slip inversions shown in **b**. **b** Aseismic slip inversion for the two months following the Huatulco earthquake. Yellow dots represent the aftershocks that occurred during the inversion time-window. Red star depicts the hypocenter of the Huatulco earthquake. Slip contours are in centimeters. Thick light gray contours are the coseismic slip shown in figure **1a**. Dashed regions are the aftershock areas for the 1978 and 1965 historic interplate earthquakes. Red and blue arrows show the observed and synthetic surface displacements, and the gray ellipses one standard deviation of the GPS displacements. Continuous and dashed arrows indicate the observed and synthetic vertical displacement, respectively.

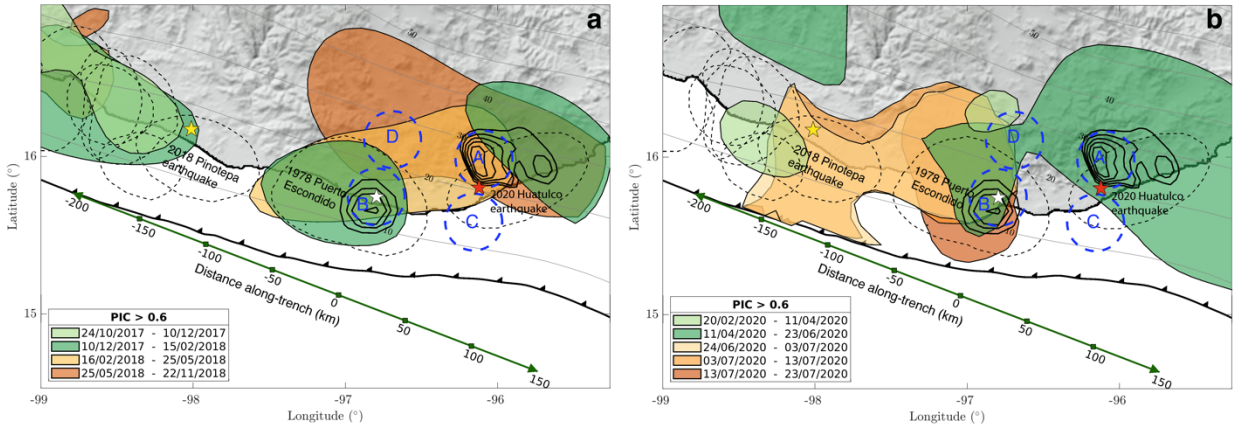

Fig. 4 Evolution of interplate strong interplate coupled regions around the rupture areas of interplate earthquakes in Oaxaca. **a** Evolution of regions with PIC > 0.6 before (green patches) and after (warm color patches) the 2018 Mw 7.2 Pinotepa earthquake. Red, orange and yellow stars indicate the hypocenter of the Huatulco, the 1978 Puerto Escondido and the 2018 Pinotepa earthquakes, respectively. Black contours represent the slip isolines of the Huatulco and 1978 Puerto Escondido earthquakes (Mikumo et al., 2002). Dashed blue circles represents the areas with radio of 20 km where we analyze the evolution of the interplate slip rate and the CFS shown in figures 6, 7c and 7d. **b** Same than **a** but for the 2020 Mw. 7.4 Huatulco earthquake. Green line indicates the along-trench profile where the evolution of the aseismic slip and CFS on the plate interface is analyzed in Figs. 5,7 and 8.

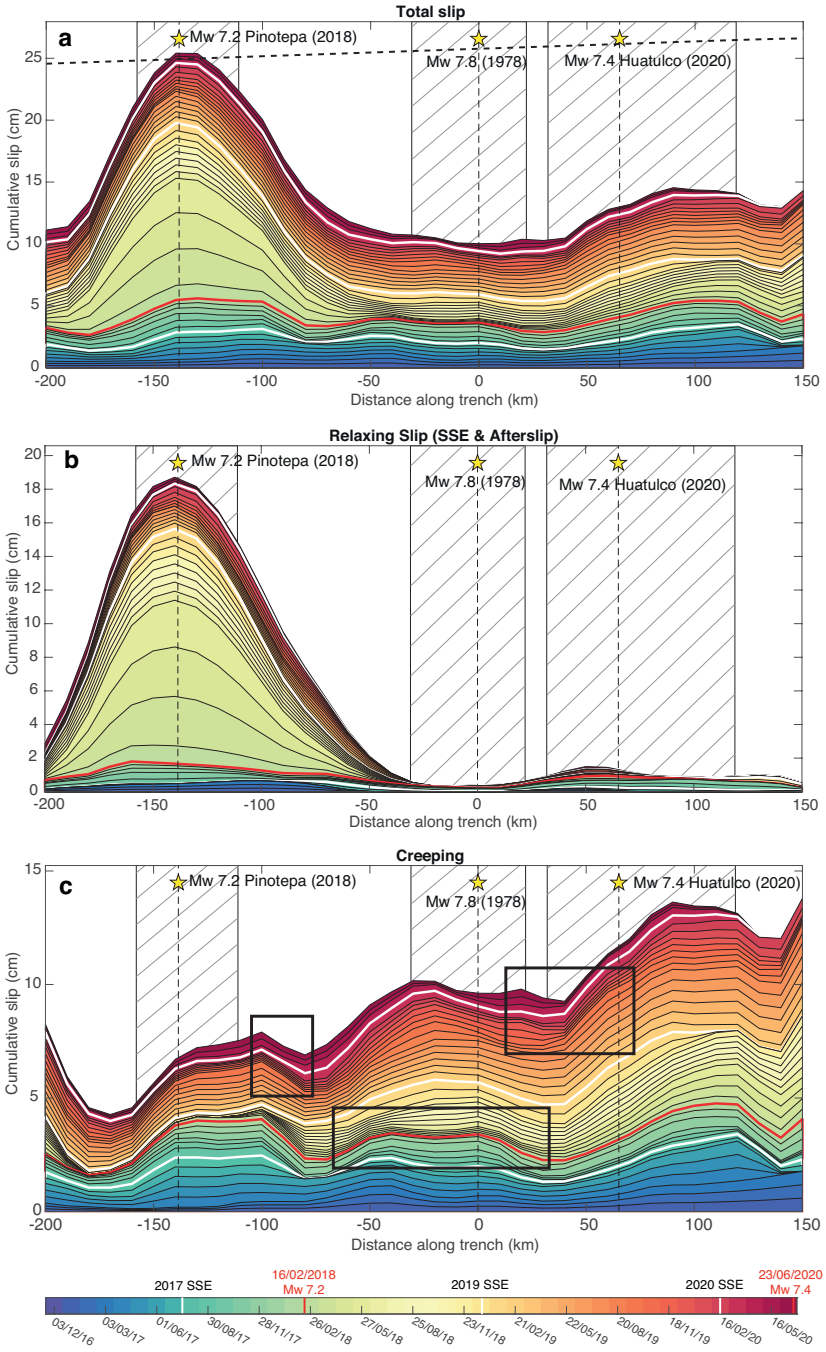

Fig. 5 Evolution of the interplate aseismic slip along the trench within the seismogenic zone of the Oaxaca subduction zone. Bottom color scale shows time. Evolution of the **a** total aseismic slip (relaxing aseismic slip + creeping), **b** the relaxing aseismic slip (SSEs and afterslip) and **c** the creeping (regions in coupling regime) averaged between 10-30 km depth. Hatched regions show the interplate segments with the highest moment release of the 2018 Pinotepa, 1978 Puerto Escondido and 2020 Huatulco earthquakes. Stars and dashed black lines indicate the along-trench coordinate of the hypocenters. White curves indicate the time when the last three long-term SSE began in Oaxaca and the red curve indicates the rupture time of the 2018 Pinotepa earthquake. Black rectangles enclose the episodes with significant variations of the slip velocity (see text). Dashed oblique line in **a** represents the expected total displacement of the incoming Cocos plate during the whole period shown by the colorbar.

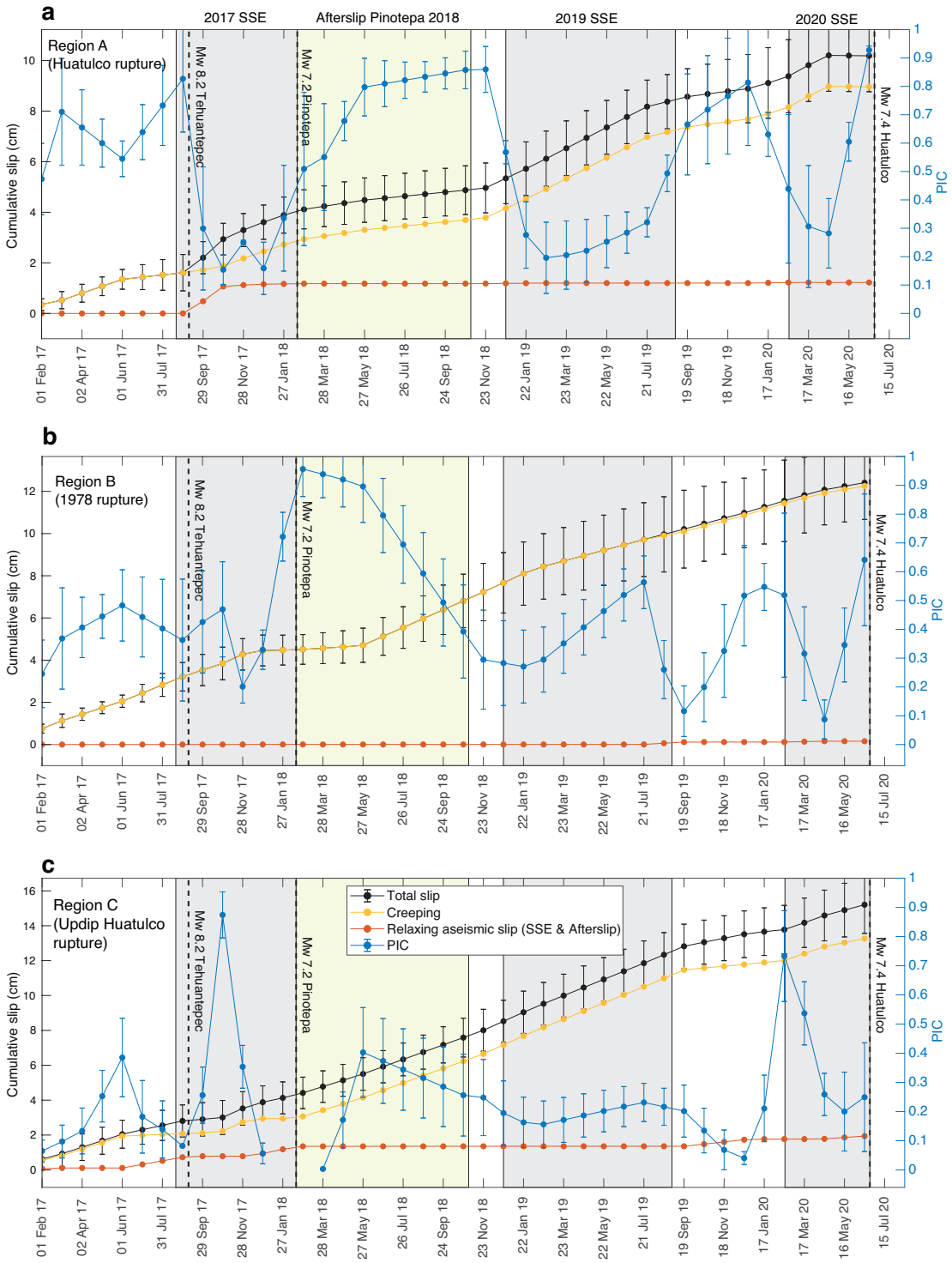

Fig. 6 Detailed evolution of the aseismic slip in the seismogenic segment of Oaxaca. Evolution of the cumulative total slip, creeping, relaxing aseismic slip and plate interface coupling in (**a**) Region A (the Huatulco rupture area), (**b**) Region B (the 1978 Puerto Escondido rupture area) and for (**c**) Region C (updip region of the Huatulco earthquake). Gray rectangles indicate the occurrence of SSEs in the region. The light-yellow rectangle shows the period when the 2018 Pinotepa earthquake afterslip developed in the region.

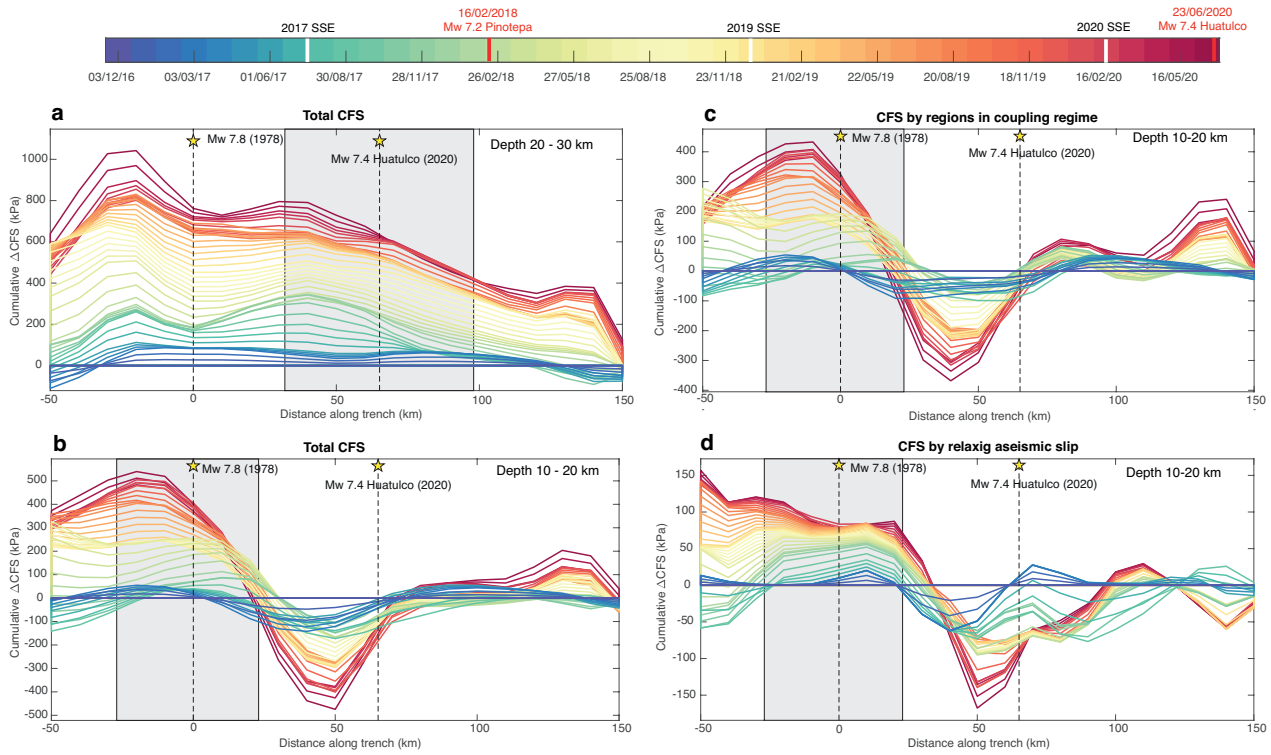

Fig. 7 Evolution of the CFS in the seismogenic segment of Oaxaca. Evolution of the total CFS along the trench for every 30 days averaged between **a** 20-30 km and **b** 10-20 km depth. Gray rectangles show the interplate segments with the highest moment release of the 2020 Huatulco earthquake and the 1978 Puerto Escondido event (Mikumo et al., 2002). **c** and **d** show the evolution of the CFS for the band between 10-20 km depth split into the contributions from regions in coupling regime and the relaxing aseismic slip, respectively.

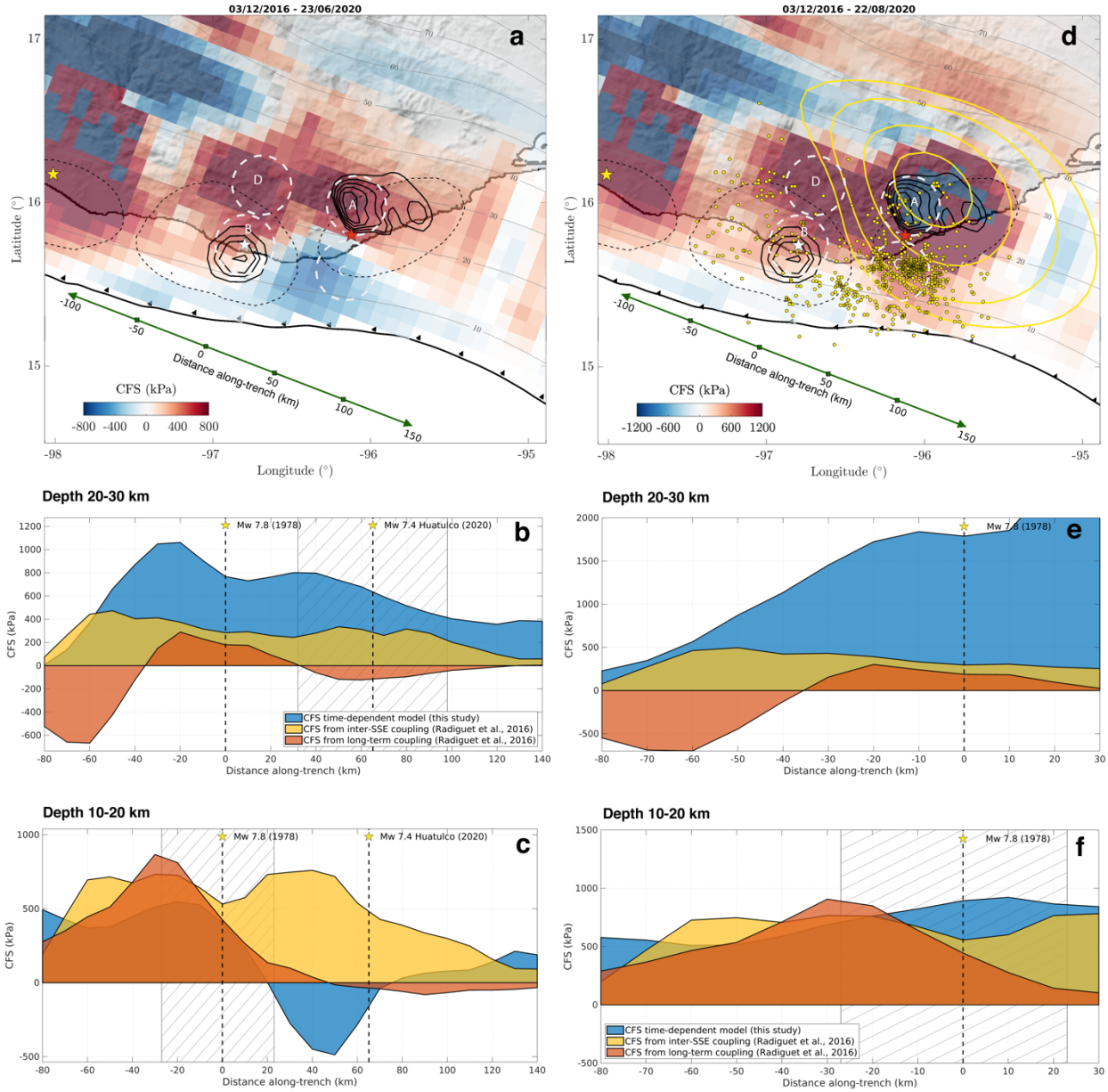

Fig. 8 Cumulative CFS from the time-variant model and its comparison with the stress built up predicted by time-invariant coupling models. **a** Cumulative CFS in the plate interface between December 2017 and the date of the 2020 Huatulco earthquake. Black contours represent the isoslip values for the 2020 Huatulco and 1978 Puerto Escondido (Mikumo et al., 2002) earthquakes. Black dashed lines delimit the aftershock areas of historic interplate earthquakes. White dashed circles represent the regions where we analyze the evolution of the interplate slip rate and the CFS shown in figures 6, 7c and 7d. **b, c** Comparison between our cumulative CFS time-variant model and the CFS predicted by time-invariant coupling models of the region (Radiguet et al., 2016) between December 2017 and the date of the 2020 Huatulco earthquake for two depth bands, between 20-30 km depth and between 10-20 km depth, respectively. **d** Same than **a** but including the stress contributions from the coseismic and postseismic phases of the Huatulco earthquake. Yellow contours are the 5,10,20 and 30 cm slip isolines of the two months cumulative afterslip. Yellow dots depict the 50 days aftershocks after the Huatulco Earthquake reported by the SSN. **e,f** Same as **b,c** but including the stress contribution from the coseismic and postseismic phases of the Huatulco earthquake focused only in the 1978 rupture segment.

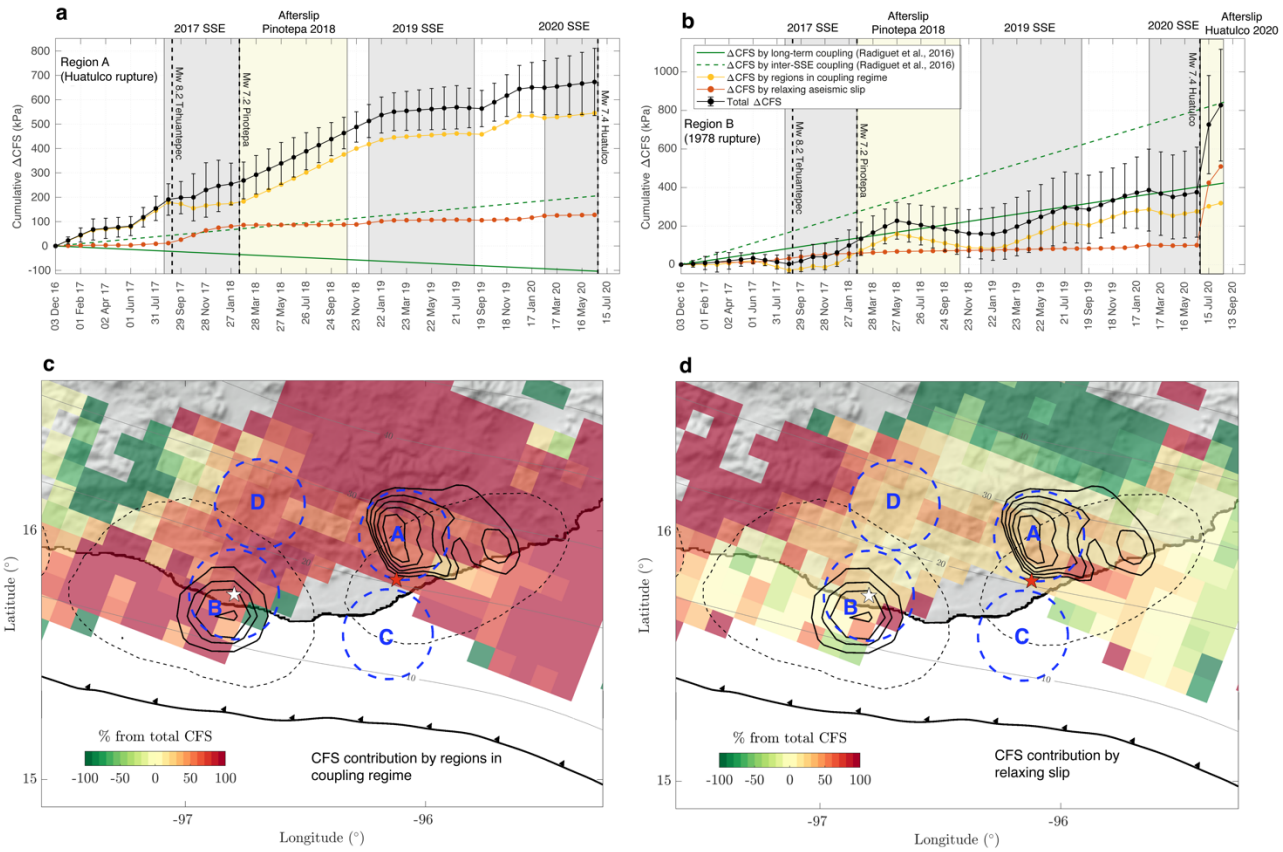

Fig. 9 CFS contributions by regions in coupling regime and relaxing slip. **a** and **b** show the evolution of the total CFS (black curves) and their contributions from the relaxing aseismic slip (red curve) and coupled regions (yellow curve), for the Region A (the Huatulco rupture area) and the Region B (the 1978 Puerto Escondido rupture area), respectively. Gray rectangles indicate the occurrence of SSEs in the region. The light-yellow rectangle shows the period when the postseismic afterslip of the 2018 Pinotepa and 2020 Huatulco earthquakes developed in the region. **c** and **d** show the CFS contributions (in %) on the plate interface where the total CFS is positive (see figure 8a) by regions in coupling regime and relaxing slip, respectively.

Supplementary Materials for:

Slow slip events and megathrust coupling changes reveal the earthquake potential before the 2020 Mw 7.4 Huatulco, Mexico, event

Authors: Carlos Villafuerte*, V. M. Cruz-Atienza, J. Tago[3], D. Solano-Rojas, R. Garza-Girón, S. I. Franco, L. A. Dominguez and V. Kostoglodov.

*Correspondence to: villafuerte.cd@gmail.com

This document includes:

Methods:

1. GNSS time series processing.
2. InSAR images processing.
3. Slip inversion method.
4. Coulomb Failure Stress estimation.

Supplementary Figures S1-S11

77 **Methods**

78

79 **1. GNSS time series processing**

80 The GNSS displacement times series are estimated using the GIPSY 6.4 software package (Lagler
81 et al., 2013), which follows a Precise Point Positioning strategy. The station positions are defined
82 in the International Terrestrial Reference Frame, year 2014 (ITRF 2014). For daily processing we
83 used the Jet Propulsion Laboratory final and non-fiducial products (orbits and clocks). We
84 generated observables using 2 model categories: (1) Earth models and (2) observation models. The
85 Earth models include tidal effects (i.e. solid tides, ocean loading and tide created by polar motion),
86 Earth rotation (UT1), polar motion, nutation and precession. Observation models, on the other hand,
87 are related with phase center offsets, tropospheric effects and timing errors (i.e. relativistic effects).
88 The troposphere delay is estimated like as random walk process. This effect is broken into wet and
89 dry components. The azimuthal gradient and the dry component are estimated using GPT2 model
90 and mapping function (TGIPSY1). The antennas phase center variations are considered through
91 antenna calibration files. For receiver antennas, the correction is estimated taking the International
92 GNSS Service (IGS) Antex file. We also applied a wide-lane phase bias to account for the
93 ambiguity resolution.

94

95 To remove the outliers and then estimate the displacement vectors per time window, we first
96 determine the data variance for each component and time window from the differences between
97 daily displacement values and a moving, locally weighted LOESS function (i.e. 2nd order
98 polynomial regressions with a half-window time support, Figs. 2a, 3a and S6). Then, all data points
99 in a time window with differences larger than one standard deviation were dismissed. Once the
00 outliers are removed, a new regression is performed to estimate the final displacement vectors.

01

2. InSAR images processing

We calculate a coseismic interferogram of the Huatulco Earthquake using two single look complex Synthetic Aperture Radar (SAR) scenes acquired by the Sentinel-1 satellites in the Interferometric Wide Swath acquisition mode, ascending pass, track 107 (Fig. S2a). The selected scenes were acquired on June 19th and June 25th, 2020, which correspond to the pair with the shortest-possible acquisition span (6 days). The pass and track were selected to provide the best-possible coverage of the coseismic signal. We use the processing chain provided in the InSAR Scientific Computing Environment (ISCE) (Rosen et al., 2012) to calculate the interferometric phase between the two SAR scenes, which includes a coarse coregistration assisted by a digital elevation model (DEM), a coarse inteferogram calculation, a fine coregistration, a fine inteferogram calculation, and basic phase corrections. Accordingly, we additionally use a 1 arc-second DEM from the Shuttle Radar Topography Mission (Farr et al., 2007) to complete the interferogram formation and topographic phase correction. Subsequently, we filter the interferometric phase using a Goldstein filter (Goldstein & Werner, 1998) to later perform phase unwrapping using SNAPHU (Chen & Zebker, 2000). We finally geocode the unwrapped interferogram, convert it to displacement in meters in line of sight (LOS) geometry and mask out water bodies and areas with spatial coherence lower than 0.4 (Fig. S2b).

Geodetic measurements from GNSS and InSAR have different reference frames, which requires converting one into the other to make a fair comparison of the displacements obtained by each technique. GNSS measurements are referenced in East, North and Up components, whereas satellite InSAR have a pixel-wise reference frame in terms of incidence (θ) and azimuth (α) angles, which vary pixel by pixel and define the relative LOS direction towards the SAR satellite. GNSS displacements can be projected onto the satellite's LOS direction following the expression (Hanssen, 2001):

$$GPS_{LOS} = -\sin\left(\alpha - \frac{3\pi}{2}\right)\sin\theta d_e - \cos\left(\alpha - \frac{3\pi}{2}\right)\sin\theta d_n + \cos\theta d_u$$

where GPS_{LOS} is the projection of the GNSS displacement vector onto the LOS vector, and d_e, d_n and d_u are the GNSS displacement components in the East, North and Up directions, respectively. Based on this transformation we adapted the ELADIN inversion method (see next section) so that the Somigliana tensor used to generate the synthetic displacements was projected into the individual LOS unit vectors per InSAR data point to perform the simultaneous GNSS and InSAR data inversion.

3. Slip inversion method

The ELADIN (ELastostatic ADjoint INversion) method (Tago et al., 2020) solves a constrained optimization problem based on the adjoint elastostatic equations with Tikhonov regularization terms, a von Karman autocorrelation function and a gradient projection method to guarantee physically-consistent slip restrictions. The method simultaneously determines the distribution of PIC and relaxing slip (i.e. SSEs and afterslip) in the plate interface to explain the surface displacements. Its precision matrix, which corresponds to the inverse of the data variance matrix (see Section 1), allows to minimize the effect of data errors (i.e. cumulative processing errors and non-tectonic physical signals) by weighting the observations. For the pre-seismic and post-seismic GNSS inversions (Figs. 2 and 3), the weights are given directly by the data variance matrix per time window and displacement component (i.e. ellipses around the tips of the horizontal displacement vectors in Figures 2 and 3) (Tago et al., 2020).

For the coseismic analysis, where GNSS and InSAR displacements are simultaneously inverted (Figs. 1 and S3c), we first inverted each data set independently. The solution using only GPS data

(Fig. S3a) describes a very simple and concentrated slip patch downdip the hypocenter with a maximum value of 4.2 m and a marginally lower than expected moment magnitude Mw 7.32 with average GPS data error of 0.2 ± 0.2 cm (Fig. S3a). The resulting model using only InSAR data (Fig. S3b) describes a more heterogeneous slip distribution with maximum value of 2.5 m and a slightly higher moment magnitude of 7.34 with average InSAR data error of 0.0 ± 1.2 cm (Fig. S3b). Then, the data weights for the joint problem were determined by trial and error until a very satisfactory solution was reached (Fig. S3c), with average GPS and InSAR data errors of 1.2 ± 1.0 cm and 0.2 ± 2.1cm, respectively. The final optimal set of values are such that all InSAR data (i.e. the 221 LOS displacements, Figs. 1b and S2c) were attributed a weight equal to one, while the GNSS data (i.e. 12 displacement components) were weighted according to the epicentral distance of each station as follows. The HUAT and OXUM sites weighed 25, the TNSJ site weighed 15, and the OXPE site weighed 5, with these values being the same in all three components per site.

Following Tago et al. (2020) and Cruz-Atienza et al., (2020), to guarantee slip restitution indexes higher than 0.5 in the whole region, we assumed a Hurst exponent of 0.75 and a correlation length of 40 km (parameters of the inverse-problem regularization von Karman function) for the pre- and post-seismic slip inversions. Also following these works, the slip rake angle could only vary 30^{o} with respect to the plate convergence direction. For the coseismic slip inversions we assumed the same Hurst exponent and determined an optimal correlation length of 7 km that allows resolving wavenumbers larger than ~50 km, which is a good compromise for imaging the main features of a M7+ earthquake. In this case we restricted the slip component perpendicular to the plate convergence direction to be smaller than 0.6 m (for details see Tago et al. (2020)).

As for the inversion exercise we performed to match the relocated hypocentral depth of 17.2 km, the results (Fig. S4) significantly improved the data fit (i.e., average errors of 0.7 $\pm$ 0.6 cm and

77 0.1 ± 1.4 cm for GNSS and InSAR data, respectively) and reproduced source characteristics similar
78 to those of our preferred solution discussed in the main text, which assumes a 3.5 km deeper
79 interface (Figs. 1a and S3c). However, it is important to point out some differences with that source
80 model: (1) the maximum slip is significantly larger (4.3 m), (2) the moment magnitude is smaller
81 (Mw 7.3) as determined from the 1 m slip contour, and (3) the rupture is more concentrated in the
82 main patch north of the hypocenter, between 18 and 30 km deep. To be consistent with the following
83 sections (i.e., to use the same interface geometry throughout the manuscript), we keep the deeper
84 solution shown in Figure 1 for subsequent analysis.
85
86
87 **4. Coulomb Failure Stress estimation**
88 The total static stress change on the plate interface is the sum of the stress contributions from plate
89 interface regions that slip, producing either a stress relaxation on the continental crust (SSEs +
90 coseismic slip + afterslip) or a stress built-up (regions in coupling regime that we modeled as
91 backslip (Savage, 1983)). To estimate the stress tensor, we discretized the 3D plate interface into
92 triangular subfaults and used the artefact-free triangular dislocation method introduced by Nikkhoo
93 and Walter (2015) for a half-space. We then compute the Coulomb Failure Stress change (ΔCFS)
94 induced on the plate interface by assuming a locally-consistent thrust mechanism following:
95
96 $$\Delta CFS = \Delta\tau + \mu\Delta\sigma_n$$
97
98 where $\Delta\tau$ represents the change of the shear stress in the direction of the fault slip (assumed to be
99 parallel to the plate convergence direction (DeMets et al., 2010); $\Delta\sigma_n$ is the change of the fault
00 normal stress (positive for tension); and μ is the apparent coefficient of friction assumed to be 0.5.
01

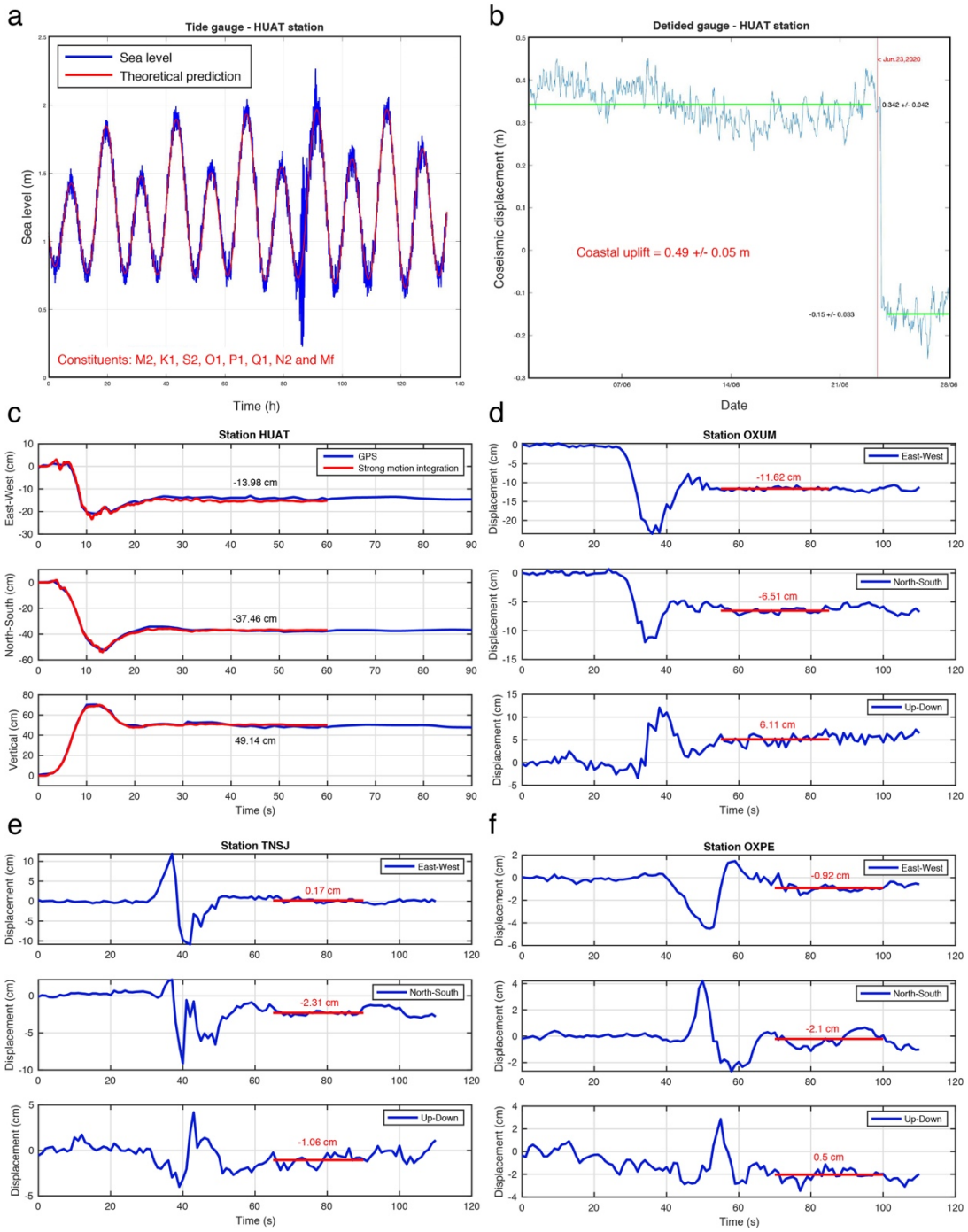

Fig. S1 Huatulco earthquake co-seismic displacements estimated from the HUAT tide gauge (**a** and **b**); high-rate GPS time series at stations HUAT (**c**), OXUM (**d**), TNSJ (**e**) and OXPE (**f**); and double integration of a strong motion record following the procedure of Wang et al. (2011)(red curve in **c**).

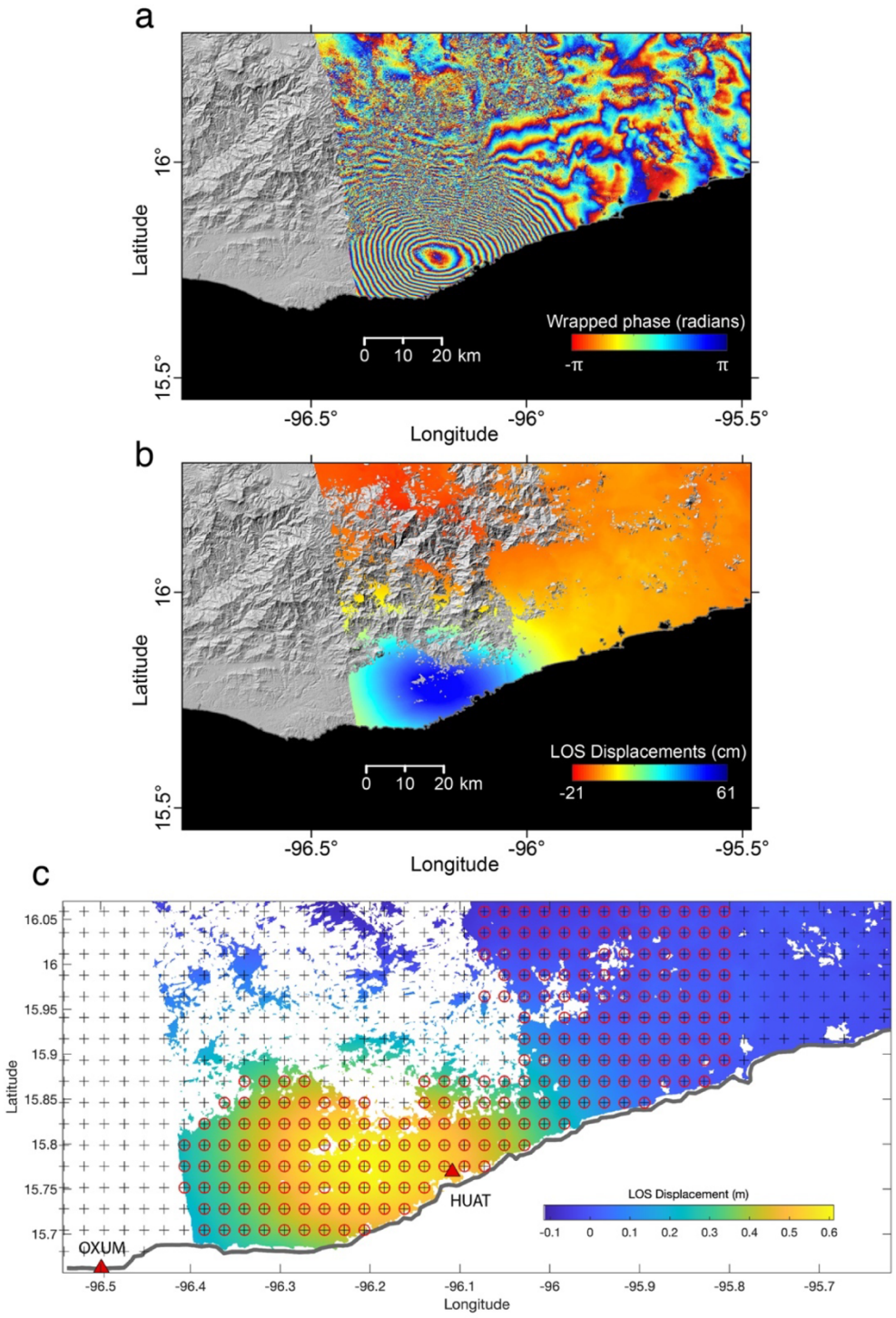

Fig. S2 Huatulco earthquake InSAR displacements estimated from Sentinel satellite images on Track 107 Ascending for scenes on June 19 and 25, 2020. **a** Wrapped phase ascending interferogram. **b** Line of sight (LOS) displacement from ascending track, positive values correspond to motion towards the satellite. **c** Same than **b** but showing the data (circles with crosses) used for the coseismic inversion.

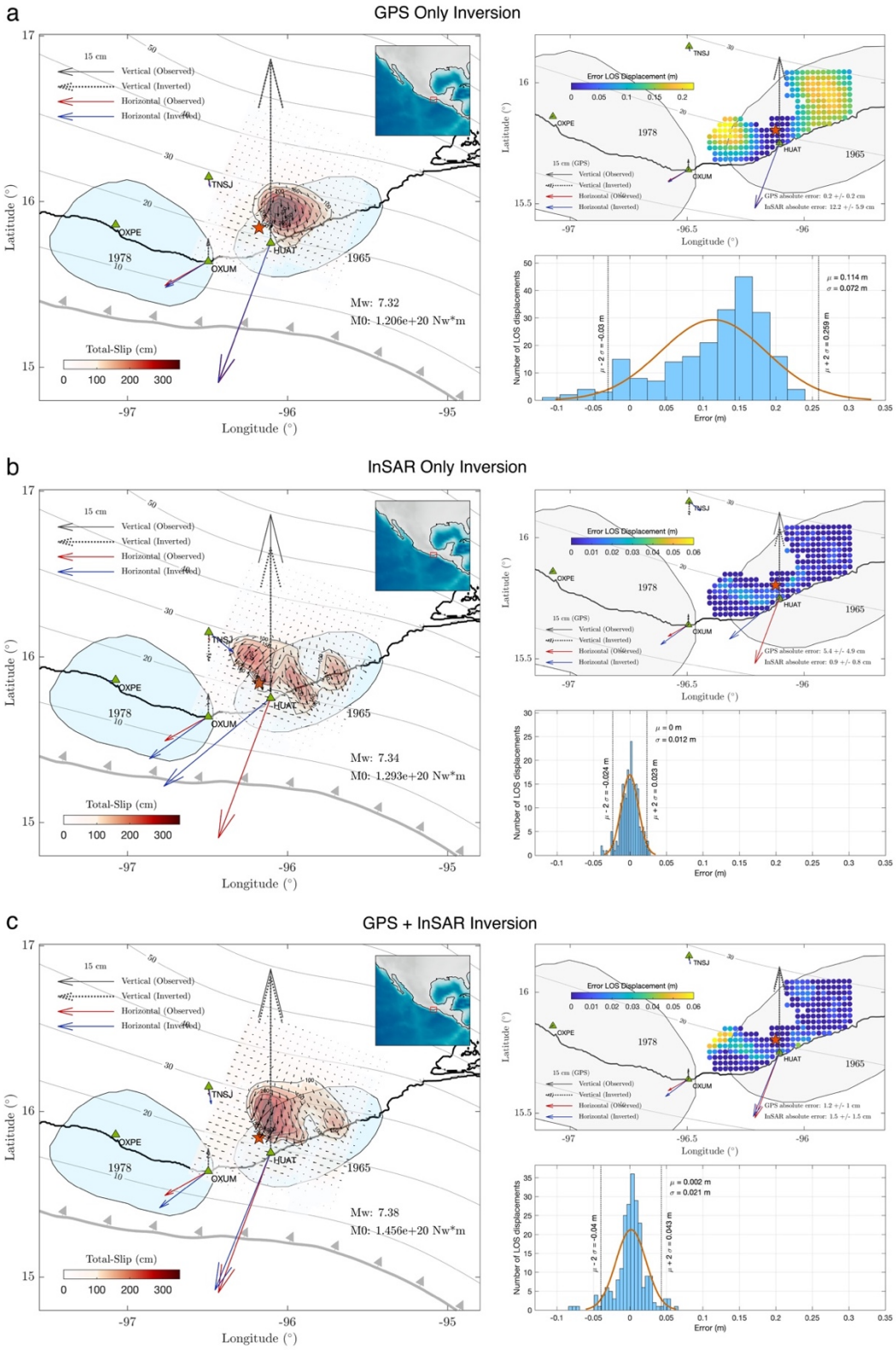

Fig. S3 Coseismic slip inversions for the Huatulco earthquake using different data sets. Coseismic slip inversion (left panel) and their associated misfit GPS and LOS displacements errors (right panels) using (**a)** only GPS data, (**b)** only InSAR data and (**c**) both GPS and InSAR data.

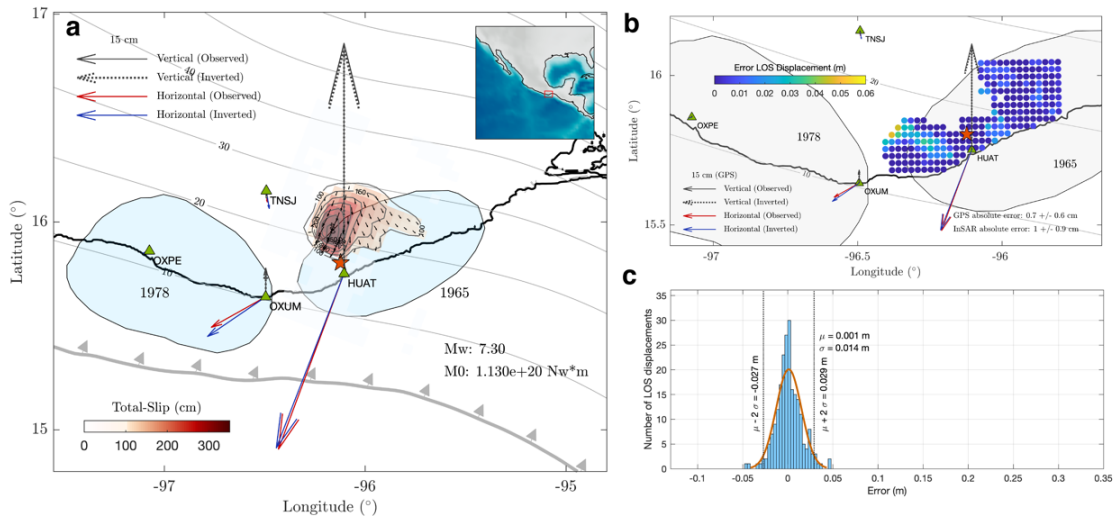

Fig. S4 Huatulco earthquake joint inversion (GNSS and InSAR) assuming that the plate interface has a depth of 17.2 km at the epicenter (i.e., shifted ~3.5 km upwards with respect to the interface shown in Figure S3). Coseismic slip inversion (**a**) and their associated misfit GPS and LOS displacements errors (**b** and **c**).

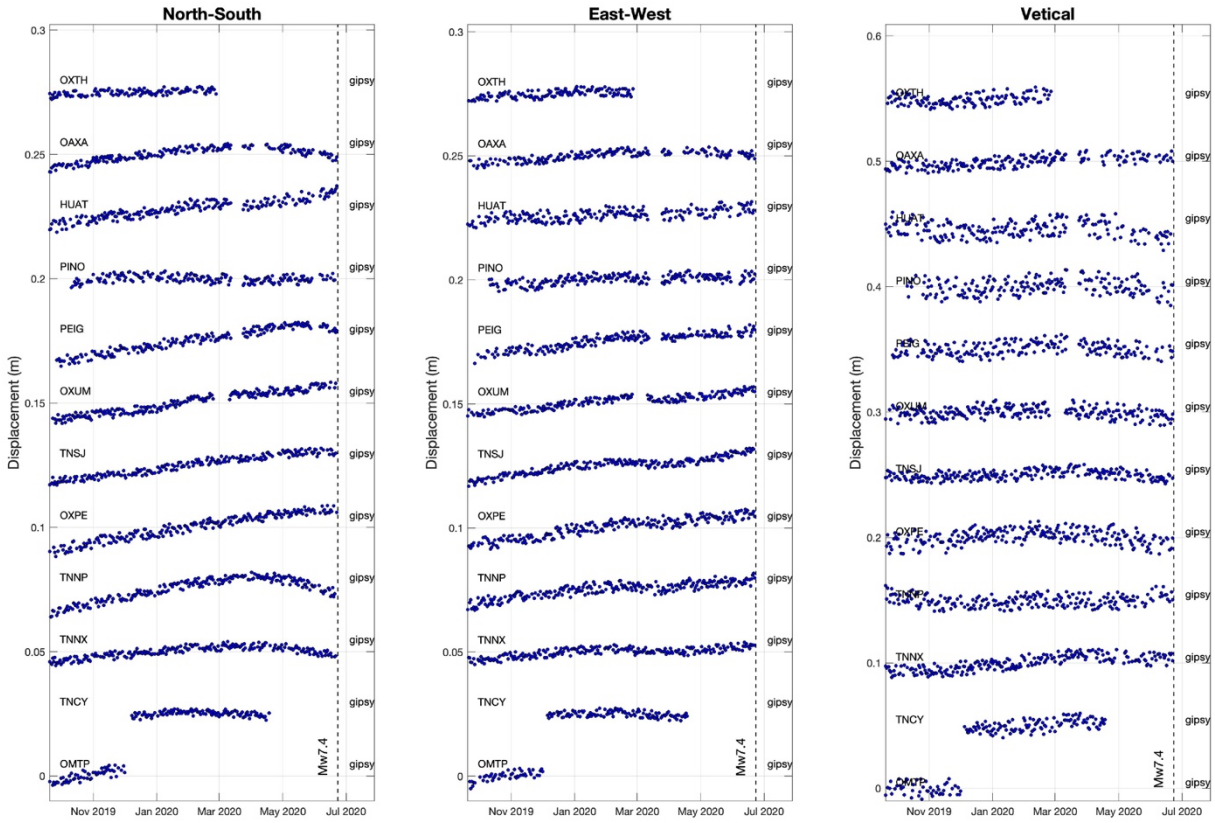

Fig. S5 GPS displacement time series estimated with the Gipsy-Oasis (v6.4) software for the pre-seismic period in the 12 stations and the three components. See Figures 2 and S6.

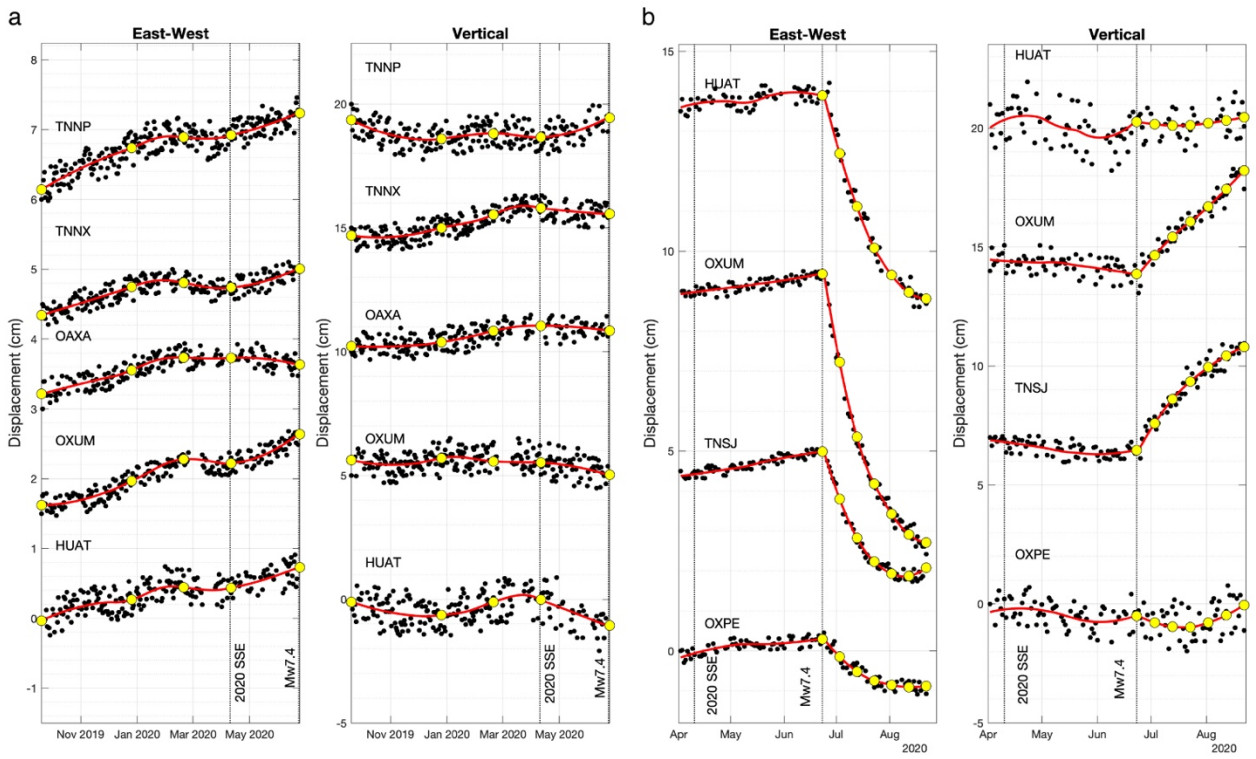

Fig. S6 East-west and vertical GPS displacement time series estimated with the Gipsy-Oasis software for the pre-seismic and post-seismic periods in selected stations shown in figures 2 and 3.

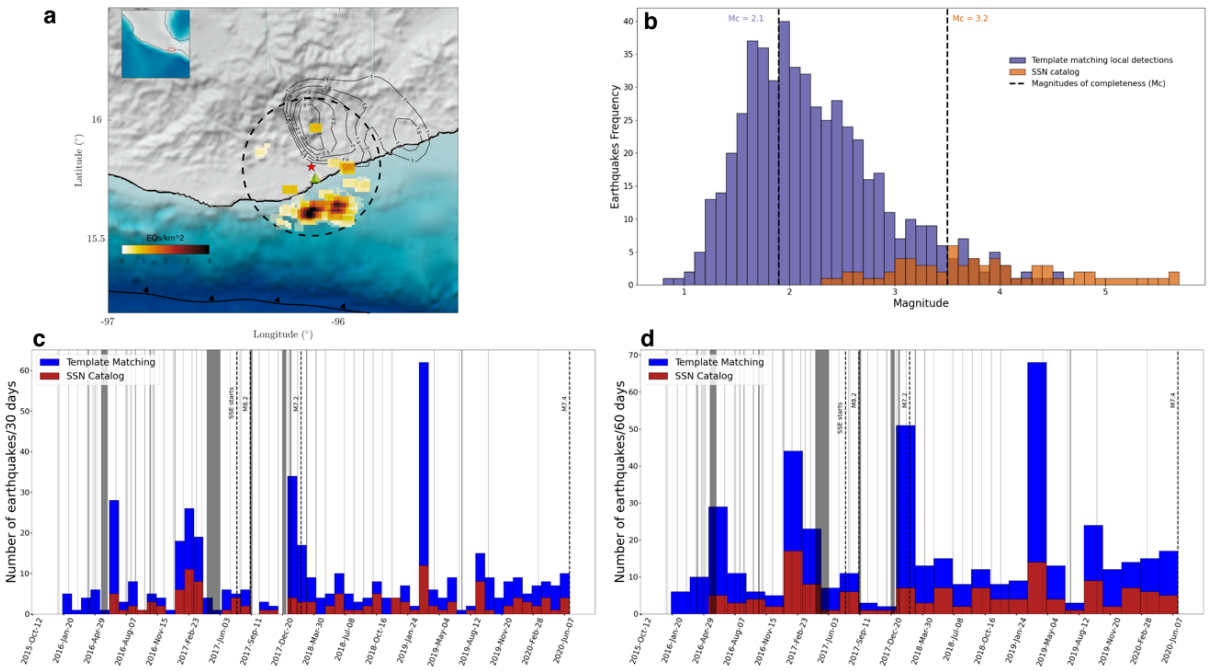

Fig S7 Illustration of template matching (TM) results using the one station method (Cruz-Atienza et al., 2020). **a** Density map of precursor TM detections using the closest station HUIG (green triangle) within 30 km from the Huatulco earthquake hypocenter (red star) and M > 2.1. Notice how almost all the detections are concentrated updip of the hypocenter due to the scarcity of templates located in the Huatulco rupture area. **b** Frequency distributions for the TM and SSN catalogs and their associated magnitude of completeness. **c**,**d** Seismicity rate evolution for the TM and SSN for two different earthquake rates. Gray sections indicate data gaps.

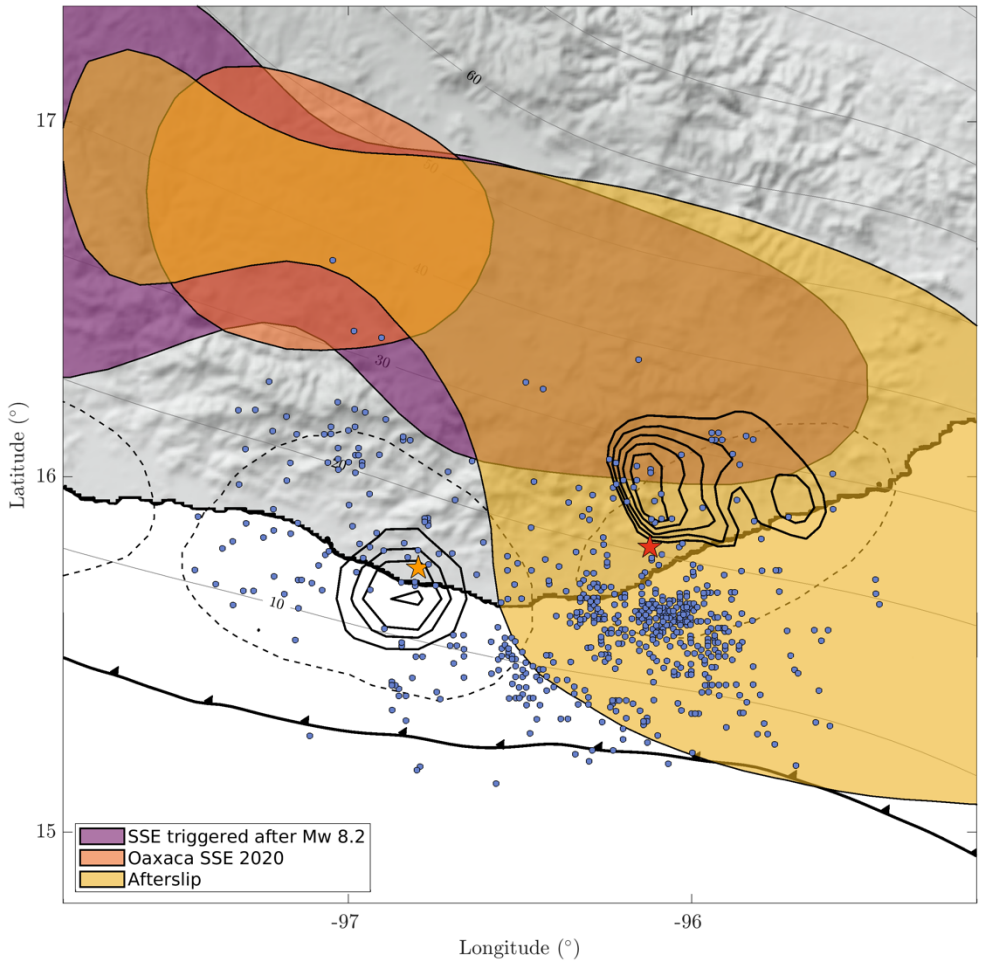

Fig. S8. Comparison of the 2017 SSE area (Cruz-Atienza et al., 2020), the coseismic slip distributions of the 2020 Huatulco (red star) and 1978 Puerto Escondido (orange star) earthquakes (black contours), the two months afterslip area following the Huatulco earthquake and the associated aftershock distribution (blue dots).

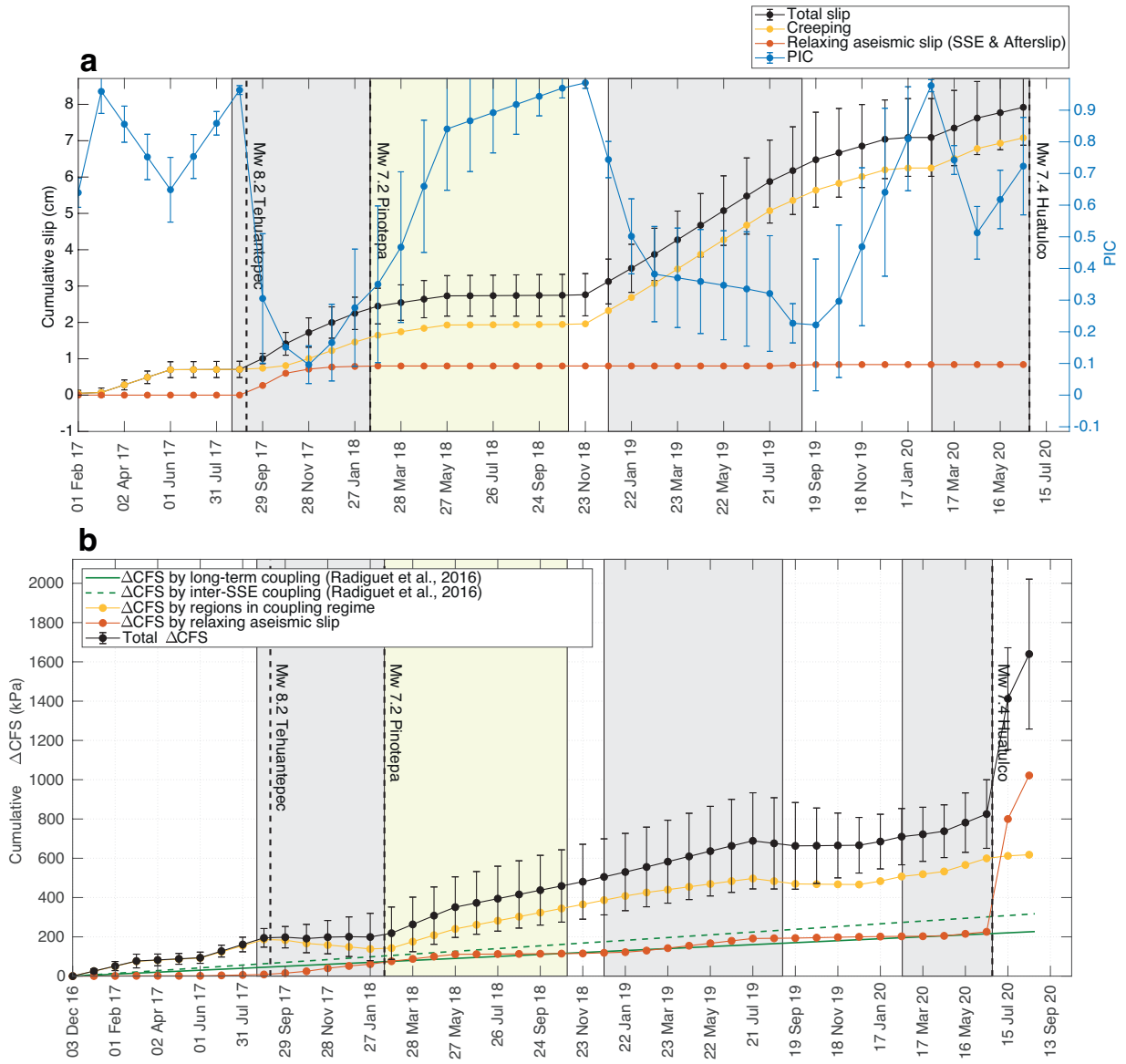

Fig. S9 Evolution of different mean quantities in Region D downdip of the 1978 rupture area (Fig. 4). **a** Cumulative total slip, creeping, relaxing aseismic slip and plate interface coupling; and **b** the total CFS and its components from relaxing slip and coupled interface regions. See Figs. 6 and 9.

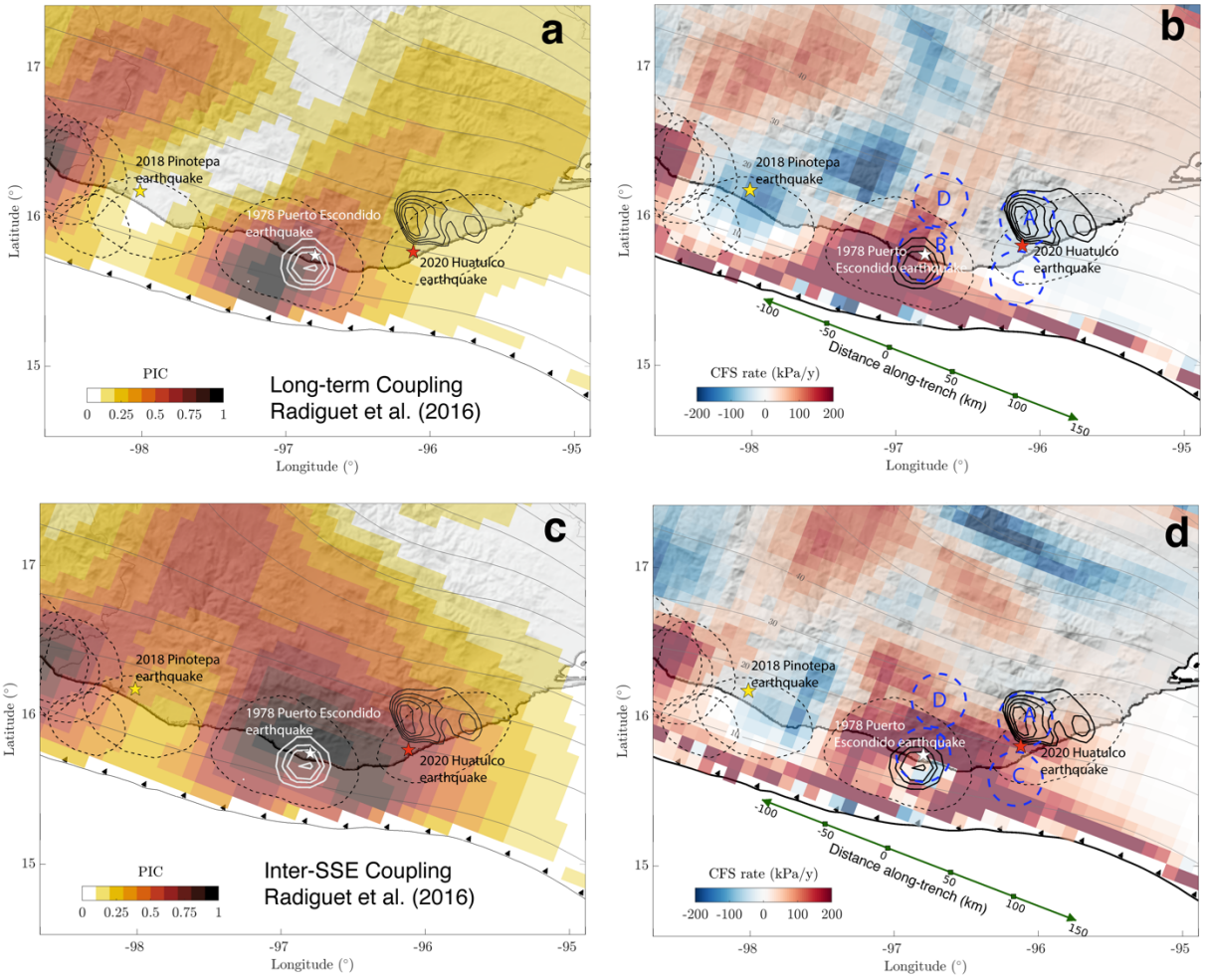

Fig. S10 Long-term and inter-SSE time-invariant interplate coupling models estimated by Radiguet et al. (2016) for the Oaxaca subduction zone and their associated CFS rates.

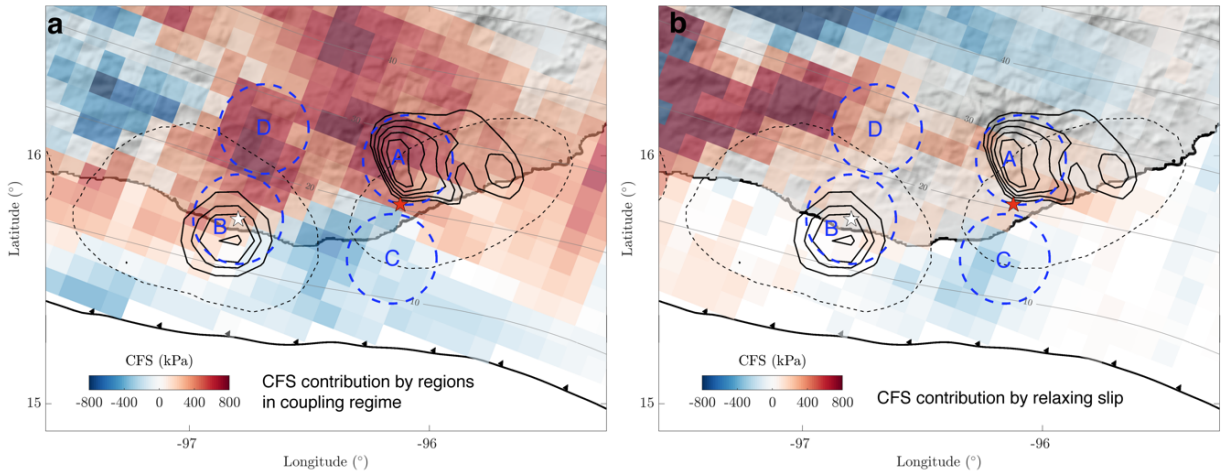

Fig. S11 Cumulative CFS contributions in the plate interface between December 2017 and the date of the 2020 Huatulco earthquake associated with regions in coupling regime (**a**) and relaxing slip (**b**).

Supplementary References

Chen, C. W., & Zebker, H. A. (2000). Network approaches to two-dimensional phase unwrapping: intractability and two new algorithms. *JOSA A*, *17*(3), 401–414.

Cruz-Atienza, V.M., Tago, J., Villafuerte, C., Wei, M., Garza-Girón, R., Dominguez, L.A., Kostoglodov, V., Nishimura, T., Franco, S., Real, J., 2020. Short-Term Interaction between Silent and Devastating Earthquakes in Mexico. Earth and Space Science Open Archive, 53.

DeMets, C., Gordon, R.G., Argus, D.F., 2010. Geologically current plate motions. Geophysical Journal International 181, 1-80.

Farr, T. G., Rosen, P. A., Caro, E., Crippen, R., Duren, R., Hensley, S., … Alsdorf, D. E. (2007). The shuttle radar topography mission. *Reviews of Geophysics*, *45*(2), 1–43.

Goldstein, R. M., & Werner, C. L. (1998). Radar interferogram filtering for geophysical applications. *Geophysical Research Letters*, *25*(21), 4035–4038. https://doi.org/10.1029/1998GL900033

Hanssen, R. F. (2001). *Radar interferometry: data interpretation and error analysis* (Vol. 2). Springer Science & Business Media.

Lagler, K., Schindelegger, M., Böhm, J., Krásná, H., Nilsson, T., 2013. GPT2: Empirical slant delay model for radio space geodetic techniques. Geophys Res Lett 40, 1069-1073.

Nikkhoo, M., Walter, T.R., 2015. Triangular dislocation: an analytical, artefact-free solution. Geophysical Journal International 201, 1119-1141.

Radiguet, M., Perfettini, H., Cotte, N., Gualandi, A., Valette, B., Kostoglodov, V., Lhomme, T., Walpersdorf, A., Cabral Cano, E., Campillo, M., 2016. Triggering of the 2014 Mw7.3 Papanoa earthquake by a slow slip event in Guerrero, Mexico. Nature Geoscience 9, 829-833.

Rosen, P. A., Gurrola, E., Sacco, G. F., & Zebker, H. (2012). The InSAR scientific computing environment. *Synthetic Aperture Radar, 2012. EUSAR. 9th European Conference On*, 730–733.

Savage, J.C., 1983. A dislocation model of strain accumulation and release at a subduction zone. Journal of Geophysical Research: Solid Earth 88, 4984-4996.

Tago, J., Cruz-Atienza, V.M., Villafuerte, C., Nishimura, T., Kostoglodov, V., Real, J., Ito, Y., 2020. Adjoint Slip Inversion under a Constrained Optimization Framework: Revisiting the 2006 Guerrero Slow Slip Event. Earth and Space Science Open Archive, 34.

Wang, R., Schurr, B., Milkereit, C., Shao, Z., Jin, M., 2011. An Improved Automatic Scheme for Empirical Baseline Correction of Digital Strong-Motion Records. Bulletin of the Seismological Society of America 101, 2029-2044.